DETECTION AND PREDICTION OF CARDIAC QUIESCENCE FOR COMPUTED TOMOGRAPHY CORONARY ANGIOGRAPHY

A Thesis
Presented to
The Academic Faculty

by

Carson A. Wick

In Partial Fulfillment
of the Requirements for the Degree
Doctor of Philosophy in the
School of Electrical and Computer Engineering

Georgia Institute of Technology
August 2014

DETECTION AND PREDICTION OF CARDIAC QUIESCENCE FOR COMPUTED TOMOGRAPHY CORONARY ANGIOGRAPHY

Approved by:

Professor David V. Anderson,
Committee Chair
School of Electrical and Computer Engineering
Georgia Institute of Technology

Professor James H. McClellan,
Advisor
School of Electrical and Computer Engineering
Georgia Institute of Technology

Professor Srini Tridandapani,
Co-Advisor
Department of Radiology and Imaging Sciences
Emory Univiersity School of Medicine

Professor John Oshinski
Department of Radiology and Imaging Sciences
Emory Univiersity School of Medicine

Professor Xiangyang Tang
Department of Radiology and Imaging Sciences
Emory Univiersity School of Medicine

Professor Omer T. Inan
School of Electrical and Computer Engineering
Georgia Institute of Technology

Date Approved: 6 May 2014

This thesis is dedicated to everyone

who helped me along the way.

TABLE OF CONTENTS

LIST OF TABLES

LIST OF FIGURES

SUMMARY

Coronary heart disease currently accounts for one in every six deaths in the United States of America [1]. Therefore, it is imperative to accurately and safely diagnose coronary artery health. The gold standard for assessing vessel health, catheterized coronary angiography (CCA), is invasive and expensive [2]. An alternative diagnostic tool, computed tomography coronary angiography (CTCA), presents a safer, more cost-effective solution as it does not require catheterization. Because the heart is a moving target, it is necessary to acquire imaging data during periods in the cardiac cycle when the heart is relatively stationary. The adoption of CTCA as a diagnostic tool has been limited by the reliability with which data acquisition can be triggered during these periods of cardiac quiescence, with mistimed acquisition resulting in blurring and other motion artifacts.

The objective of this work is to improve the diagnostic quality and reduce the radiation dose of CTCA imaging by developing gating techniques based on signals derived from cardiac motion, rather than the currently used electrocardiogram (ECG), to more reliably trigger data acquisition during periods of cardiac quiescence. Because the ECG is an indication of electrical activity, it is a surrogate marker of the mechanical state of the heart. Therefore, gating based on a signal derived directly from cardiac motion using either echocardiography or seismocardiography (SCG) should prove better at detecting and predicting periods of cardiac quiescence. Improved gating would permit the use of CTCA in more instances to either replace or determine the necessity of invasive and expensive CCAs.

This work presents novel methods for detecting and predicting cardiac quiescence.

Quiescence is detected as periods of minimal velocity from echocardiography, computed tomography (CT), and SCG. Identified quiescent periods are used to develop and evaluate techniques for predicting cardiac quiescence using echocardiography and SCG. Both echocardiography and SCG are shown to be more accurate for predicting quiescent periods than ECG. Additionally, the average motion during quiescent periods predicted by echocardiography and SCG is shown to be lower than those predicted using only ECG. Lastly, cardiac CT reconstructions from quiescent phases predicted by a commercial CT scanner were compared to the optimal quiescent phases calculated using the CT quiescence detection methods presented in this work. The diagnostic quality of the reconstructions from the optimal phases was found to be higher than that of the phases predicted by the CT scanner, suggesting that there is the potential for marked improvement in CTCA performance through more accurate cardiac gating.

The remainder of this document is organized as follows. Chapter 1 provides an introduction to coronary angiography (CA), including a brief background on the modalities used in this work. In Chapter 2, the methods developed to detect cardiac quiescence are presented. Chapter 3 presents the methods for predicting cardiac quiescence for CTCA. A brief discussion on the impact and applications of this work for CTCA is given in Chapter 4. Lastly, Chapter 5 gives guidance for future work on this topic.

CHAPTER I

INTRODUCTION

CA is a vital tool for diagnosing coronary vessel disease. The most widely used method, CCA, relies on cardiac catheterization of the patient followed by an injection of contrast agent and a biplanar x-ray. An alternative method, CTCA, eschews catheterization, using a computed tomography (CT) approach. Magnetic resonance imaging (MRI) can also be used for CA in a similar manner to CTCA. Although MRI-based CA can accurately identify coronary arteries without ionizing radiation, it is currently less sensitive in detecting vessel stenosis than CTCA [2,3]. In addition to being noninvasive, CTCA provides true three-dimensional images of not only the coronary vasculature, but also of the adjacent heart. Because of the physiological constraints of CT, data acquisition is non-instantaneous and sensitive to cardiac motion. As a result, the effects of cardiac motion on image quality need to be mitigated. This can be accomplished by more accurately triggering data acquisition during periods of cardiac quiescence, by improving the temporal resolution of CTCA, by pharmacologically suppressing the heart rate of the patient, or by using advanced reconstruction techniques.

1.1 Background of the Modalities Used in this Work

A brief overview and background of each of the sensing modalities used in this work are provided in this section. Should the reader already be familiar with any of these modalities, individual sections may be skipped.

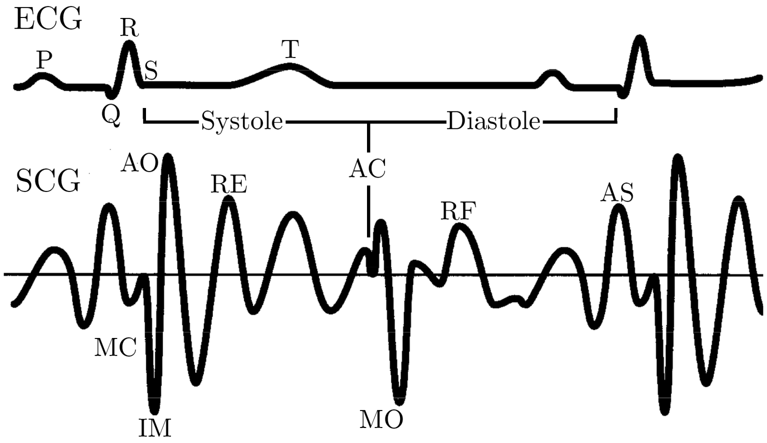

Figure 1: Signal features of the ECG (top) and SCG (bottom). For the SCG, the features corresponding to the mitral valve closing (MC), isovolumic movement (IM), aortic valve opening (AO), rapid ejection (RE), aortic valve closing (AC), mitral valve opening (MO), rapid filling (RF) and atrial systole (AS) are shown. Figure reproduced from [5].

1.1.1 Electrocardiography

ECG provides a recording of the electrical activity of the heart. Pioneered by Einthoven in the early 1900s, ECG is still the predominant method for diagnosing many cardiac conditions, primarily those concerning cardiac rhythm [4]. The readily identifiable features of the ECG, shown in Figure 1 along with those of the SCG, make it extremely useful for determining the timing of the electrical activity of the heart. When segmentation of cardiac cycles is necessary, a pair of successive R-peaks of the ECG, an R-R interval, is often used to define the beginning and end of the cardiac cycle. As a measure of the electrical activity of the heart from electrodes placed on the skin surface, the ECG is an excellent indicator of the electrical health and function of the heart.

1.1.2 Seismocardiography

SCG provides a recording of the acceleration of the chest wall due to cardiac motion. The use of acceleration as an indicator of cardiac function can be traced back to

1939 when Starr first published on ballistocardiography, the measurement of gross hemodynamics from the force exerted by the patient on a ballasted table [6]. The interest of the medical community in ballistocardiography waned with the development of echocardiography as a more accurate method for assessing cardiac function but interest has recently seen an uptick [7]. As a measurement of localized acceleration due to cardiac motion, the SCG has also seen increased interest with the development of smaller accelerometers that can be placed more conveniently on the chest. SCG as a measurement of precordial acceleration was first described in literature by Salerno et. al in 1990 [8]. Since then it has been shown to be useful for assessing cardiac mechanics and function [9–11]. A typical SCG and the features corresponding to specific cardiac events are shown in Figure 1 along with a corresponding ECG signal.

1.1.3 Echocardiography

Echocardiography provides a recording of the heart using ultrasound interrogation. Based on ultrasonic techniques developed from the mid-1930s to the mid-1950s, the initial implementation of echocardiography took place in 1953 by Edler and Hertz [12]. Echocardiography image reconstruction relies on the timing and intensity of reflected ultrasonic pulses emitted and received from an ultrasound transducer probe. Obtaining high quality echocardiographic images is generally more difficult than other ultrasound images due to the presence of ribs. Ultrasonic pulses do not penetrate bone, and thus, the placement of the ultrasound transducer is constrained to intercostal spaces between the ribs, referred to as acoustic windows.

There are three important echocardiographic techniques, among others, for assessing cardiac dynamics: B-mode, M-mode, and tissue Doppler imaging (TDI). B-mode echocardiography refers to a sequence of two-dimensional echocardiographic images, from which cardiac dynamics can be observed. M-mode imaging is used to view cardiac dynamics of a sequence all at once. A single line trace of imaging data is

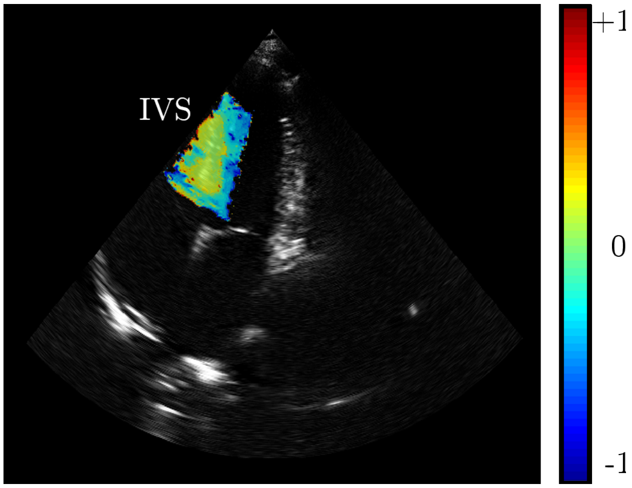

Figure 2: Example of a B-mode echocardiography frame with the normalized color TDI velocity of the IVS shown. Positive (red) values indicate motion toward the transducer.

reconstructed and displayed for each time instance. This results in a two-dimensional data set, depth by time, allowing for cardiac dynamics along the M-mode trace to be readily observed as a single image. TDI records cardiac tissue velocity in the direction parallel to that of ultrasound interrogation, determined by the Doppler frequency shift of the received ultrasonic pulses. Color TDI refers to localized velocity measurement overlaid on a B-mode sequence with color representing tissue velocity. An example of a B-mode frame and the corresponding color TDI data for the inter-ventricular septum (IVS) is provided in Figure 2. As a direct, real-time indication of the heart, echocardiography is an excellent tool for assessing cardiac motion.

1.1.4 Cardiac Computed Tomography

CT provides a graphical representation of internal structures of the body. The first clinical CT scan was conducted in 1972 by Hounsfield of EMI laboratories [13]. Cardiac CT relies on taking sufficient x-ray line projections through the volume to be imaged so that an image of the heart can be reconstructed. These projections, collectively a CT acquisition, should ideally occur while the heart is in the same position.

This poses a unique challenge in triggering acquisition during a specific quiescent period of the cardiac cycle, generally for multiple beats. The utility of cardiac CT was initially limited due to cardiac motion, however, as CT technology progressed and temporal resolution increased, cardiac CT has become a powerful diagnostic tool [14].

1.1.4.1 CT Problem Formulation

CT aims to reconstruct an image from multiple x-ray projections through the interrogated volume. The ratio of the emitted and received x-ray intensity can be used to approximate the line integral of the intensity—the localized attenuation coefficients—of the desired image along that line path. This relationship is summarized as $p = ln(I_e/I_r)$ where p approximates the line integral and I_e and I_r are the emitted and received x-ray intensity, respectively. The mathematics behind this inverse problem are largely accredited to Radon who developed his transform in 1917, though work on a three-dimensional formulation was carried out by Lorentz in 1905 [14]. For the brief treatment of CT acquisition and reconstruction to follow, the discussion is constrained to the single-slice, two-dimensional reconstruction problem. For a more thorough treatment of three-dimensional reconstruction please refer to [15] or [13]. Let $f(x, y)$ be the desired two-dimensional image intensity function in cartesian coordinates and $L(\ell, \theta)$ be the straight line in $\mathbb{R}^2$ with an orthogonal projection to the origin of length ℓ and angle θ. Then, the Radon transform is defined as

$$p(\ell, \theta) = \iint f(x, y)\delta(x \cos\theta + y \sin\theta - \ell)dxdy, \tag{1}$$

where $p(\ell, \theta)$ is the Radon transform of $f(x, y)$ and δ is the Dirac delta function. Note that $\delta(x \cos\theta + y \sin\theta - \ell)$ is equal to one along $L(\ell, \theta)$ and zero elsewhere, resulting in $p(\ell, \theta)$ being equal to the line integral of $f(x, y)$ along $L(\ell, \theta)$. Therefore, a CT x-ray projection taken along $L(\ell, \theta)$ will correspond to $p(\ell, \theta)$ of the Radon transform of the desired image, $f(x, y)$. As a result, the Radon transform space, $(\ell, \theta) \in \mathbb{R}^2$, can be populated by taking multiple x-ray projections through the volume to be imaged. Because the line integral should be the same regardless of which direction the x-ray beam passes through the body, π radians will adequately cover the θ dimension of the Radon transform space. Mathematically, this is because $p(\ell, \theta) = p(-\ell, \theta + \pi)$. Hounsfield originally sampled π radians at $\pi/180$ radian intervals, taking 160 laterally translated projections per angle interval. This sampling density was adequate to reconstruct an 80 × 80 image [13].

Reconstruction algorithms rely on the inverse Radon transform defined as

$$f_{polar}(r, \phi) = \frac{1}{2\pi^2} \int_0^{\pi} \int_{-E}^{E} \frac{1}{r\cos(\theta - \phi) - \ell} \frac{\partial p(\ell, \theta)}{\partial \ell} d\ell d\theta, \tag{2}$$

where $p(\ell, \theta)$ is the Radon transform of the desired image, $f_{polar}(r, \phi)$, in standard polar coordinates and $\pm E$ is the range of lateral translations over which acquisitions were acquired. The desired image can be expressed in cartesian coordinates as $f(x, y)$ using the relation $x = r\cos\phi$ and $y = r\sin\phi$. Many algorithms exist for solving (2), including filtered backprojection, algebraic reconstruction techniques, and quadratic optimization methods [15].

1.1.4.2 Cardiac CT Data Acquisition

Phase selective cardiac CT using conventional scanners became feasible in the 1990s due to technological advances increasing the temporal resolution of CT imaging [14]. Cardiac CT currently relies on a synchronously acquired ECG signal to select the cardiac period during which CT projections are acquired. Two modes of acquisition are commonly used for cardiac CT, helical scanning and step-and-shoot.

Helical scanning for phase selective cardiac CT is most commonly associated with retrospective gating, described in Section 1.3.1.1. The basic concept of helical scanning is to slowly move the patient along the longitudinal axis while the gantry rotates about the patient. If the patient is chosen as the frame of reference the path of the emitter will follow a helical path centered around the longitudinal axis of the patient.

To reduce radiation dose, emitted x-ray intensity is modulated based on the ECG so that maximum intensity is delivered during phases of predicted cardiac quiescence.

Step-and-shoot (SAS) acquisition of cardiac CT data is used for prospective gating as described in Section 1.3.1.2. SAS acquisition and reconstruction is simpler than helical scanning in that the patient table is not moving during acquisition. SAS became feasible with the advent of multi-slice scanners capable of acquiring a substantial volume in one acquisition. The name SAS describes the protocol, i.e., the table *steps* in the longitudinal direction then the scanner *shoots* to acquire data. The process is repeated until the entire cardiac volume is imaged. SAS is currently gated using the ECG so that the *shoot* portion occurs while the heart is predicted to be quiescent and the *step* portion takes place during phases of large cardiac motion. SAS relies on accurate prediction of cardiac quiescence so that cardiac motion is actually minimal during acquisition. Cases with elevated heart rate variability make ECG-based quiescence prediction extremely difficult, limiting the performance of prospectively-gated SAS acquisition [16]. Because x-ray emission is not continuous, SAS methods result in much less radiation exposure for the patient than helical scanning [17, 18].

1.2 Methods for Coronary Angiography

The first selective coronary angiogram was performed in 1958 when Sones unintentionally injected contrast agent, intended for the aorta, directly into the right coronary artery [2]. Until this point it was feared that such a direct injection of contrast would lead to dangerous cardiac arrhythmias or even death. Since then, the CCA technique has become the *de facto* standard for assessing coronary vessel health. CTCA was first introduced by Moshage et al. in 1995 as a noninvasive alternative to CCA that does not require catheterization [19]. The diagnostic quality of CTCA has improved with advances in CT technology and improved image reconstruction techniques, though cardiac motion still presents a distinct challenge. As shown in Figure 3, diagnostic

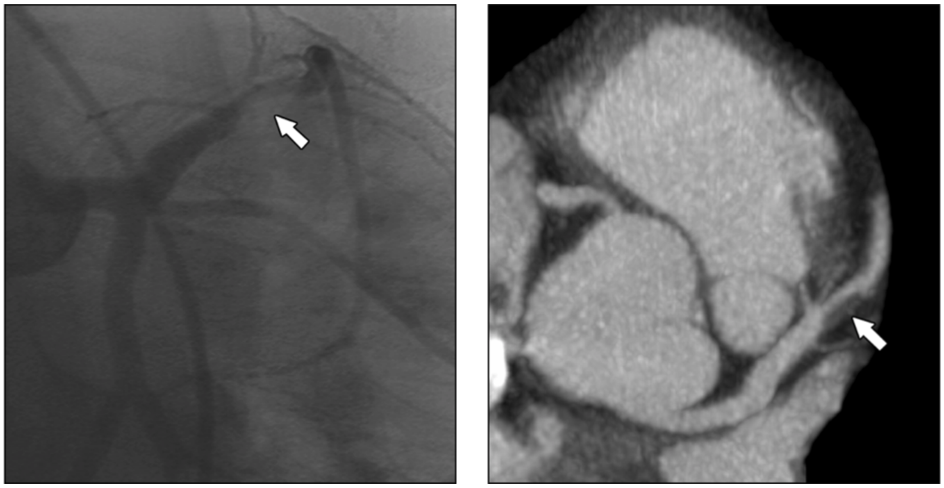

(a) CCA (b) CTCA

Figure 3: Diagnostic images of the same coronary vessel stenosis using both CCA and CTCA for a single patient. Images reproduced from [20].

images of the same vessel stenosis can be obtained for a single patient using both CCA and CTCA methods.

1.2.1 Catheterized Coronary Angiography

CCA is currently the gold standard for assessing coronary artery health [2]. CCA provides high-resolution images of the coronary vessels, both spatially and temporally, with data for each image being acquired in 3-10 ms [21]. However, this resolution comes at a cost. Because CCA requires catheterization, the imaging modality is both expensive and invasive. More than one million CCA exams are performed annually in the United States of America costing approximately $40 billion and resulting in more than 14,000 major complications [1]. Though these complications have decreased in recent years, they still present a non-trivial risk [22]. Furthermore, roughly 40% of CCAs reveal no coronary artery disease [23].

A CCA exam begins with a catheter tube being fed through the circulatory system and into the heart. The femoral artery is the most common entry point, though the radial artery is gaining in popularity [2,24]. After the end of the catheter is positioned in the desired coronary artery, contrast agent is injected. A sequence of biplanar x-ray images is then taken to observe the flow of contrast agent through the coronary vessels. The three-dimensional interior structure of the vasculature can be approximated using the two sequences of synchronously acquired x-ray images, though this technique is still sensitive to vessel overlap and foreshortening [25]. In addition, CCA does not provide any indication of the vessel wall structure or general cardiac anatomy.

Coronary vessel health is diagnosed by observing vessel narrowing. The coronary vessels are visible due to the contrast agent impeding x-ray transmission through the interior volume of the vessel, as shown in Figure 3(a). As a result, changes in the interior dimensions of the coronary arteries can be investigated by observing the flow of contrast through the vessels.

1.2.2 CT Coronary Angiography

CTCA is a relatively new technique wherein angiography is performed using a conventional CT scanner. Because heart motion is cyclical in nature, gating of data acquisition can be performed to trigger acquisition during periods of minimal cardiac motion. This gating is either done retrospectively or prospectively. For retrospective gating, data is acquired continuously during the exam and only afterwards the periods for reconstruction are chosen. Prospective gating relies on a triggering system, currently based on the ECG, to selectively acquire CT data during cardiac cycle periods of expected quiescence. Because acquisition is selective, prospective gating results in much less radiation dose than retrospective gating [17,18]. Additional information on cardiac gating methods is provided in Section 1.3.1. An added benefit of CTCA over CCA is that a true three-dimensional representation of the vasculature is obtained. In addition, myocardial tissue is imaged providing ancillary information regarding the cardiac structure of the patient.

The major constraint of CTCA is temporal resolution. Acquiring enough CT data

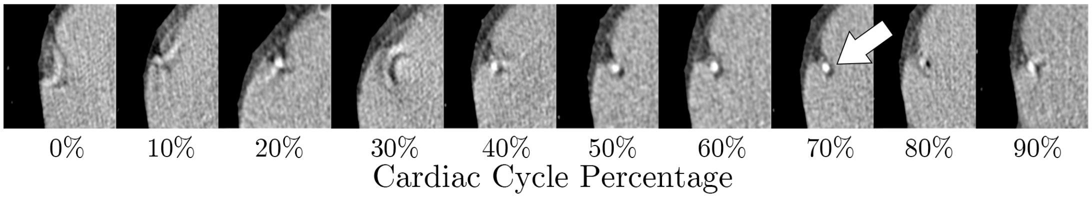

Figure 4: Example of CTCA motion artifacts of the RCA as a function of cardiac phase. The reconstruction centered at 70% of the cardiac cycle, the approximate location of the diastolic quiescent period, provides the best diagnostic quality. Images provided by Drs. S. Tigges and G. Sirineni, Department of Radiology, Emory University.

to reconstruct images of the heart takes time. In fact, the modern era of CTCA only began in the mid-1990s due to advances in CT technology reducing data acquisition durations to less than those of cardiac quiescent periods [26, 27]. If the heart moves during acquisition, motion artifacts will occur as shown in Figure 4 for images of the right coronary artery (RCA) reconstructed at 10% intervals throughout the cardiac cycle. For this example, the diagnostic quality of the RCA can be seen to vary and that the reconstruction from the period centered at 70% provides the highest quality image. Though modern CT equipment has lowered the acquisition time, cardiac motion remains the primary obstacle in obtaining diagnostic quality images of coronary vessels.

1.3 Techniques to Mitigate the Effects of Cardiac Motion on CTCA

Cardiac motion during CTCA acquisition can lead to either non-diagnostic images or worse, incorrect diagnostic measurements [28, 29]. The effects of cardiac motion can be mitigated by cardiac gating to acquire data during periods of cardiac quiescence, decreasing CTCA acquisition time, lowering the heart rate pharmacologically with β-blocker medication, or by using advanced cardiac CT reconstruction algorithms. It is important to note that these techniques are not mutually exclusive and can be used together for increased improvement in CTCA imaging performance.

1.3.1 Cardiac Gating of Data Acquisition

The most straightforward method for minimizing the effect of cardiac motion on image quality is to avoid it altogether. Retrospective and prospective gating techniques are both used to reconstruct CTCA images from data acquired during periods of presumed cardiac quiescence. For retrospective gating, CTCA data is acquired continuously throughout the cardiac cycle and the cardiac phase providing the best reconstruction is identified post acquisition. For prospective gating, the optimal phase is predicted during acquisition and is represented as a delay from some feature in the cardiac gating signal, currently the R-peak of the ECG.

1.3.1.1 Retrospective Gating

For retrospective gating techniques, data is acquired continuously and reconstructions can be made throughout the cardiac cycle. This allows for the optimal cardiac period for reconstruction to be chosen from the set of all cardiac phases. These periods were originally chosen manually based on image quality, though now they can be identified automatically [30]. Because the data used for reconstruction is chosen after the scan, retrospective acquisition is less sensitive to gating mistiming and heart rate variability than prospective gating. The tradeoff for this robustness is an increase in radiation dose. Though the x-ray tube current, and hence the received radiation, is modulated depending on the cardiac cycle phase, the radiation dose for retrospective gating methods remains much larger than that of prospective gating methods [17,18].

1.3.1.2 Prospective Gating

The goal of prospective gating is to acquire data only during periods of cardiac quiescence. The current method for predicting quiescent periods is based on the ECG signal. ECG-based gating of data acquisition begins with real-time detection of the R-peaks of the ECG signal. The heart rate of the the patient is then estimated using

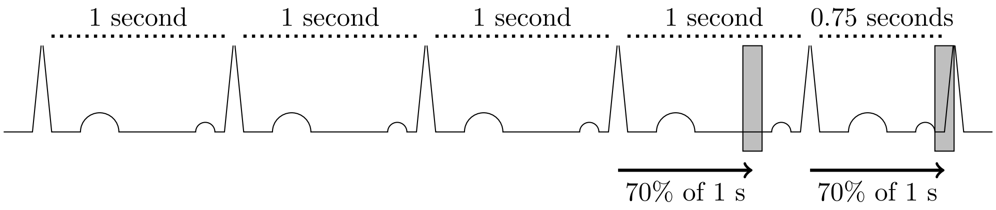

Figure 5: Example of real-time prospective ECG-based gating and the difficulties associated with heart rate variability. Grey bars indicate CT acquisition delayed from the previous ECG R-peak by 70% of the predicted cardiac cycle length. The predicted cycle length is estimated from the R-R intervals of the preceding cycles. For the last cycle, this results in severely mistimed CT acquisition due to heart rate variability.

the R-R interval of some number of preceding cycles. Lastly, after some heart-rate-dependent cycle-percentage delay from the R-peak, CT data acquisition is triggered. This process is summarized in Figure 5 where the R-peaks used to estimate the heart rate and trigger acquisition are shown. This sequence has a nominal heart rate of 60 beats per minute which corresponds to a desired ECG trigger delay of roughly 70% of the cardiac cycle. A shorter cardiac cycle that could be attributed to heart rate variability follows the first triggered acquisition to highlight the difficulties associated with quiescent period prediction and cardiac gating associated with heart rate variability.

Currently, ECG-based prospective gating is generally only advised for patients with heart rates less than 75 beats per minute and low heart rate variability [16, 31]. This is due to the shorter quiescent periods associated with higher heart rates and the difficulties in prediction associated with high heart rate variability. To increase the robustness of prospective gating, CT data acquisition time is often padded, i.e., additional acquisition time is added to the beginning and end of the predicted quiescent period to allow for a small amount of flexibility during reconstruction. Although this padding increases the radiation dose, selective prospective gating dosage is still much less than that of retrospective methods [17, 18].

1.3.2 Improved CTCA Temporal Resolution

The detrimental effects of cardiac motion on image quality can be decreased by shortening the time needed to acquire sufficient data for image reconstruction. Data acquisition speed can be increased by rotating the CT gantry at a higher rate, by acquiring many slices at the same time, or by using multiple x-ray sources. Together, these methods have reduced the time necessary for CT acquisition from five minutes to less than a second for the most advanced multi-slice scanners [27].

1.3.2.1 Decreased Gantry Rotation Time

Since the first clinical CT scan in 1972, the medical community has seen a decrease in CT gantry rotation time from roughly 300 seconds to 0.27 seconds [14]. Temporal resolution is inversely related to gantry rotation time and has consequently seen a proportionally equivalent increase. There are currently two primary factors limiting the further increase in gantry rotation speed, centripetal acceleration and power constraints. Current CT scanners operating at maximum speed experience acceleration upwards of 30 G (gravitational constant). Thus, a further increase in gantry rotation speed poses a very challenging design problem. The second obstacle is powering the x-ray tube(s). Because power is a function of the square of the tube current, the power necessary to deliver equivalent radiation exposure increases with the square of rotational velocity of the gantry. As an example, sub-200 ms gantry rotation times would require approximately 200 kW of power during acquisition [14].

1.3.2.2 Multi-slice Methods

CT imaging initially acquired only one image slice at a time. As x-ray emitter and detector array technology has advanced, the number of simultaneously acquired slices has increased greatly, with the current maximum being 320 slices [27]. An increase in the number of slices results in a corresponding increase in the volume imaged during one acquisition. Consequently, the number of acquisitions required to image the entire heart decreases as the number of simultaneously acquired slices increases, resulting in a decrease in total scan time.

1.3.2.3 Dual-source CT

A CT acquisition with a single x-ray source requires a gantry rotation of 180° to adequately sample the volume to be imaged as described in Section 1.1.4. Therefore, an acquisition for a single-source CT requires half the time necessary for a full gantry rotation. Dual-source CT scanners, introduced in 2005 [32], feature two sources offset from each other by 90°. This results in a required rotation of only 90° to obtain all possible projections necessary for reconstruction, consequently halving the acquisition time.

1.3.3 Pharmacological Heartrate Suppresion

β-adrenergic antagonists, commonly referred to as β-blockers, are often administered prior to CTCA acquisition to lower the heart rate of the patient. β-blockers have been shown to improve image quality for patients with elevated heart rates above 75 beats per minute [16]. By lowering the heart rate of the patient, quiescent periods associated with lower heart rates can be used for CTCA acquisition. The nature of quiescent periods for lower heart rates is useful for both retrospective and prospective gating, though, β-blockers are generally not necessary for retrospective reconstruction.

The benefits of lowering the heart rate do not come without caveats as β-blockers can cause serious cardiopulmonary complications [33, 34]. Asthma and other obstructive pulmonary conditions are the most common contraindications. In addition, β-blockers can aggravate certain medical conditions, including aortic or carotid stenosis. Because these conditions can be undiagnosed for those receiving a CTCA exam, extreme care must be taken before prescribing β-blocker medication for heart rate suppression.

1.3.4 Advanced Cardiac CT Reconstruction Techniques

Rather than attempting to solve the cardiac motion problem in a physical sense, advanced reconstruction techniques can be used to reduce the effect of cardiac motion on CTCA. These can be broken down into techniques to perform motion compensation during image reconstruction and techniques to perform reconstruction from less data, resulting in an increase in effective temporal resolution.

The goal of motion compensation techniques is to identify cardiac motion and incorporate it into the reconstruction process. In general, a continuous CT scan is completed and a coarse reconstruction of the entire cardiac cycle is performed. From this reconstruction the cardiac motion is estimated as a function of the cardiac cycle, relative to the R-R interval of the ECG. This motion information is then used to compensate for cardiac motion during reconstruction. This is necessary for periods of the cardiac cycle where motion is large as each angular view is recorded at a slightly different time and, subsequently, phase of the cardiac cycle. Methods for motion estimation, motion compensated reconstruction, and the combination of the two are an active area of research [35–38].

Techniques for reconstruction using an otherwise insufficient amount of data can improve temporal resolution by shortening the gantry rotation necessary to accurately reconstruct images. One promising method leveraging recent signal processing advances in compressive sensing is temporal-resolution-improved prior-image-constrained compressive sensing [39–42]. This technique uses a reconstruction from a standard acquisition to constrain a second reconstruction using only a small subset of the views taken for the standard acquisition. This method has shown an initial doubling in the temporal resolution of cardiac CT while still maintaining spatial accuracy.

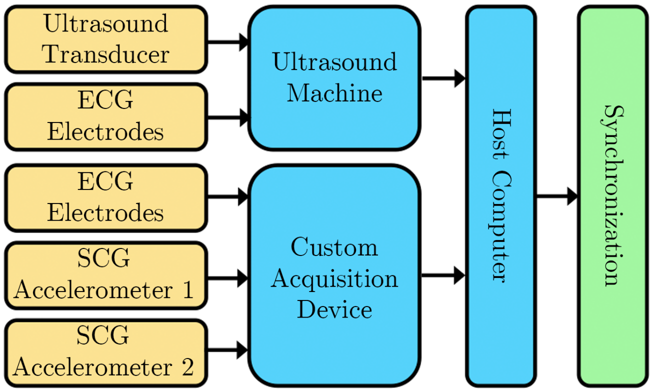

Figure 6: Hardware system overview. The redundancy of the ECG signals from both a custom device and the ultrasound machine allows for temporal synchronization across all three modalities.

1.4 Synchronous Acquisition System

To investigate the efficacy of cardiac-motion-based signals for detecting and predicting cardiac quiescence for CTCA, it is first necessary to synchronously acquire those signals. To that end, a complete hardware system was developed to acquire synchronous ECG, SCG, and echocardiography data [43], as shown in Figure 6. The ultrasound machine used for echocardiography is a SonixTOUCH Research scanner (Analogic, Peabody, MA, USA) capable of acquiring raw B-mode, M-mode, TDI, and ECG data. In conjunction with the ultrasound machine, a custom hardware device is used to acquire synchronous SCG and ECG data. The ECG signal, common to both the ultrasound system and the custom hardware system is used for synchronization. The data rates of each data type are provided in Table 1.

1.4.1 Custom SCG Acquisition Device

A custom SCG acquisition device is used to synchronously acquire both ECG and SCG data at high rate and precision (1.2 kHz, 16-bit). As shown in Figure 7, the device consists of an ECG channel and two SCG channels. Multiple SCG channels allow for multiple simultaneous SCG signal acquisitions from different locations. An additional motivation for using a custom solution is that most commercial accelerometer devices

Table 1: Data Rates for the Synchronous Data Acquisition System

Data Source	Data Type	Data Rate
Custom Device	ECG Data	1.2 kHz
Custom Device	SCG Data	1.2 kHz
Ultrasound Machine	B-Mode Data	30 fps
Ultrasound Machine	M-Mode Data	83 Hz
Ultrasound Machine	TDI Data	17 Hz
Ultrasound Machine	ECG Data	200 Hz

do not feature analog DC-offset removal prior to digitization. DC offset removal is critical for the SCG channels as the amplitude of the SCG acceleration is very small in comparison to the gravitational acceleration of the earth. By removing the large constant offset due to gravity from the accelerometer channels, effectively centering the signal at zero magnitude, the gain can be greatly increased so that the SCG signal uses the full dynamic range of the analog-to-digital converter (ADC). Without the tunable gain and DC-offset compensation, the accuracy of the SCG data would be decreased significantly due to ADC quantization error associated with digital signals that have small magnitude relative to the dynamic range of the system. DC offset compensation also has the added benefit of removing most of the respiratory motion from the SCG.

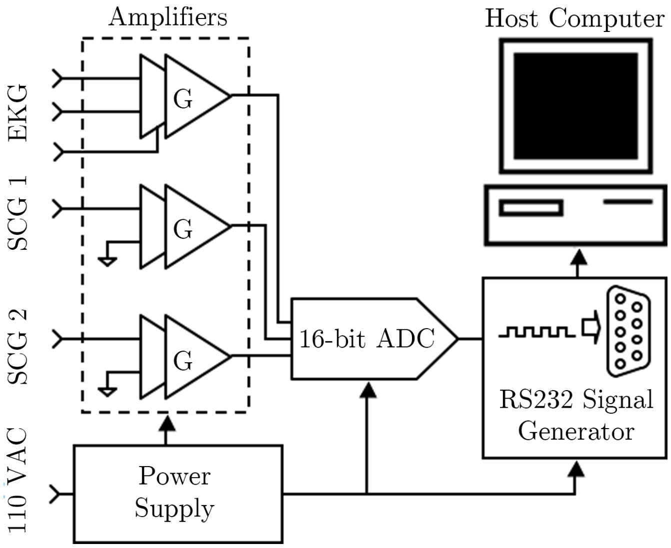

Figure 7: Simplified schematic of the custom device to synchronously acquire an ECG and two SCG data streams.

CHAPTER II

DETECTION OF CARDIAC QUIESCENCE

Quiescent periods of the cardiac cycle are detected using echocardiography, CT, and SCG. The motivation for observing quiescence from each of these modalities is varied. B-mode echocardiography provides two-dimensional motion information of the heart on a beat-by-beat basis. For this reason, quiescence of the IVS observed from B-mode echocardiography will serve as the baseline to assess the performance of the quiescence prediction methods detailed in Chapter 3. Cardiac CT provides full three-dimensional motion information of the heart at a higher spatial resolution than B-mode echocardiography. However, cardiac CT requires multiple heart beats to reconstruct three-dimensional volumes and thus cannot be used to observe cardiac quiescence on a beat-by-beat basis. Cardiac CT will be used to establish the relationship between the coronary vessels, not readily observable from echocardiography, and the IVS, which can be observed from echocardiography. Lastly, SCG provides a measure of the motion of the chest wall due to cardiac activity. Because the SCG is acquired from a small sensor that does not require operator involvement during recording, it is a CT compatible modality whereas B-mode echocardiography generally is not. Thus, SCG will be used to investigate potential real-time, CT-compatible cardiac gating techniques. In addition, the use of SCG as a potential method for obtaining patient-specific gating parameters from a convenient and inexpensive test prior to CTCA examination will be explored.

2.1 Echocardiography-Based Quiescence Detection

Quiescent periods are detected from B-mode echocardiography on a beat-by-beat basis using a robust correlation-based deviation measure. Echocardiography is used to investigate quiescence due to its real-time nature, high temporal resolution, accessibility, and lack of ionizing radiation. In particular, because echocardiography directly provides cardiac motion information, it allows for the accurate assessment of cardiac quiescence on a beat-by-beat basis. B-mode echocardiographic data consists of a sequence of two-dimensional images, allowing for the application of image processing methods, and provides insight into the in-plane, two-dimensional motion of the heart as a function of time. Echocardiographic tissue Doppler imaging (TDI) is often used for measuring the velocity of cardiac tissue in the direction of ultrasound interrogation. TDI relies on the Doppler shift of the received ultrasonic pulses to calculate tissue velocity. While TDI is an efficient, straightforward measurement of cardiac motion, it is only sensitive in the direction of the ultrasonic pulse and therefore cannot capture the two-dimensional motion that can be derived from B-mode data.

2.1.1 Methods for Echocardiography-Based Detection

To better understand and more accurately predict quiescent periods, the interventricular septum (IVS) is observed using frame-to-frame deviation measurement techniques and active contour based tracking. The IVS was chosen because it has been shown to be an accurate indicator of cardiac and, importantly for CTCA, coronary vessel quiescence [44].

2.1.1.1 Frame-to-Frame Deviation Measurement Methods

The underlying cause of motion blur is movement during data acquisition. If the heart is stationary for some period of a B-mode sequence, the image content of each frame during that period will be similar. In this sense, frame-to-frame dissimilarity—*deviation*—can be associated with movement and hence consecutive frames with low deviation correspond to cardiac quiescence.

Deviation between frames is expressed as a negative function of the Pearson correlation coefficient taken over the IVS as it has been shown to be a strong indicator of image similarity [45]. Here, the Pearson correlation can be thought of as a measure of the similarity between two frames and is defined as

$$\rho(i,j) = \frac{\sum\limits_{(x,y)\in I} (I_i(x,y) - \overline{I}_i)(I_j(x,y) - \overline{I}_j)}{\sqrt{\sum\limits_{(x,y)\in I} (I_i(x,y) - \overline{I}_i)^2 \sum\limits_{(x,y)\in I} (I_j(x,y) - \overline{I}_j)^2}} \tag{3}$$

where I_i is frame i, $\overline{I}_i$ is the mean of I_i, and (x,y) indexes each frame.

The correlation-based, frame-to-frame deviation measure is calculated from a user-selected static rectangular region containing the IVS. For this work the region was selected by a graduate researcher and verified by a physician. This process could be automated if necessary [46]. The deviation calculation of the region of interest (ROI) is summarized as

$$\begin{aligned} \mathbf{D}(i,j) &= 1 - \rho(i,j) \\ &= 1 - \frac{\sum\limits_{(x,y)\in S} (I_i(x,y) - \overline{I}_i^S)(I_j(x,y) - \overline{I}_j^S)}{\sqrt{\sum\limits_{(x,y)\in S} (I_i(x,y) - \overline{I}_i^S)^2 \sum\limits_{(x,y)\in S} (I_j(x,y) - \overline{I}_j^S)^2}} \end{aligned} \tag{4}$$

where I_i is frame i, S is the constant rectangular image region over which correlation is calculated, $\overline{I}_i^S$ is the mean of I_i in S, and (x,y) indexes each frame. S is chosen so that the cardiac feature of interest is contained in S for all frames. This is accomplished by observing the beginning of the B-mode sequence for at least one cardiac cycle.

Frame-to-frame deviation measurements for all possible comparisons of frame pairs for a given B-mode sequence are calculated according to (4) and recorded as a *deviation matrix*, $\mathbf{D}(i,j)$, where i and j are the time indices of the two frames being compared. When viewed as an image, this allows for the frame-to-frame deviation of the entire sequence to be efficiently observed, as shown in Figure 8(a) for one cardiac cycle.

Quiescence from Deviation Measures Cardiac quiescence occurs when velocity is minimal. In turn, this corresponds to low deviation between neighboring frames in the cardiac sequence. Thus, square regions of low deviation along the diagonal of the deviation matrix, $\mathbf{D}(i, j)$, indicate cardiac quiescent periods. The process of calculating the timing and duration of these periods is automated. For each point along the diagonal of $\mathbf{D}(i, j)$, the mean deviation measure of a square neighborhood centered at that point is calculated. The size of this neighborhood is increased until the mean deviation is no longer below a specified threshold, the mean of $\mathbf{D}$ in this case. Here the *quiescence*, $q(i)$, for each time instance, i, is defined as the duration of the gating window centered at i indicated by the width of the largest square region centered at $\mathbf{D}(i, i)$ with mean deviation below the specified threshold as shown in Figure 8. This method can be seen as an extension of the one-dimensional, M-mode method presented in [47] to two-dimensional B-mode data.

Quiescent Periods from Velocity Approximation The magnitude of the two-dimensional velocity of the IVS can be approximated from the deviation matrix because $\mathbf{D}(i, j)$ can be shown to be linear with feature displacement. This linearity holds under the assumptions that the feature does not deform and that the motion is linear between frames i and j, as described in Appendix A. Given the B-mode sampling period of 20 to 30 ms, these assumptions are reasonable for neighboring frames. Therefore, $\mathbf{D}(i, i-1)$ is approximately proportional to the velocity magnitude of the IVS within a scaling factor and constant offset. The approximated velocity, defined as

$$\hat{v}_{echo}(i) = \mathbf{D}(i, i-1), \tag{5}$$

is normalized and expressed in arbitrary units, allowing inter-subject comparisons to be made. The approximated velocity, $\hat{v}_{echo}(i)$, can be fit to a reference velocity so that it can be expressed in cm/s if needed. This process is summarized in Appendix A by (47), (48), and (49).

Quiescent periods of the cardiac cycle are identified as intervals when $\hat{v}_{echo}(i)$ is

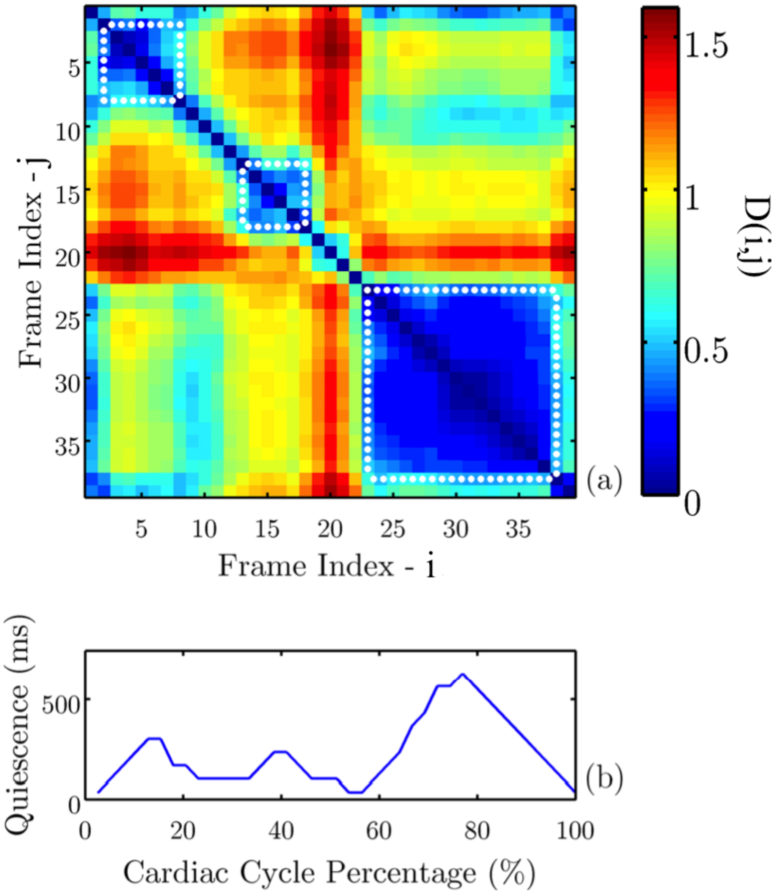

Figure 8: Graphical representation of echocardiography-based quiescence detection from the deviation matrix, $\mathbf{D}$ (a), and the corresponding quiescence plot, q (b). One cardiac cycle is shown with a period of 1.2 seconds. Quiescent periods are indicated by dotted white squares where the mean value of $\mathbf{D}$ was chosen as the threshold.

less than the mean of $\hat{v}_{echo}(i)$. This choice of threshold was made to facilitate the comparison of quiescent periods from different echocardiographic sequences.

Interpolated velocity maps expressed in arbitrary units are calculated to assist in the visual identification of cardiac quiescent periods as shown in Figure 9. The velocity of each cardiac cycle, segmented by the R-peaks of the synchronously acquired ECG signal, is normalized to have a minimum of zero and a mean of one. This choice was made to eliminate the dependence on the maximum velocity, which was observed to vary more than the minimum and mean between cycles and acquisitions. Cubic interpolation is used to fit the data to a uniform grid, allowing velocity to be displayed

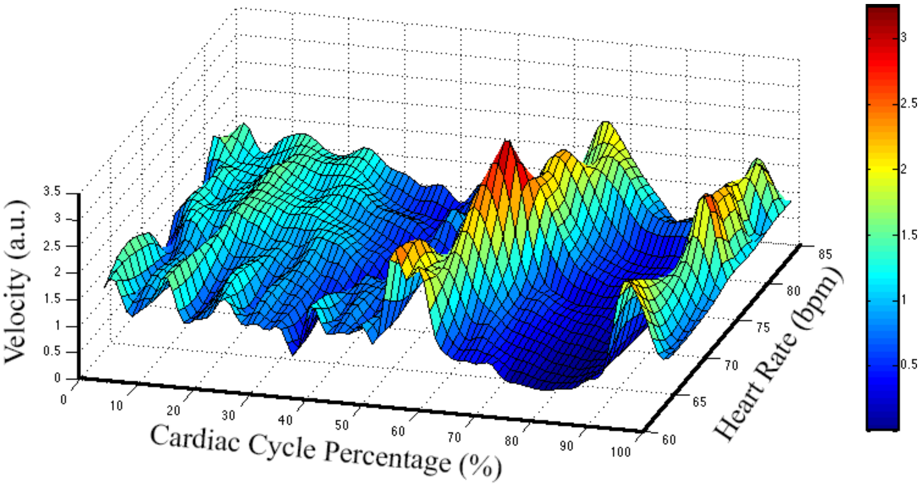

Figure 9: Interpolated velocity map from $\hat{v}_{echo}(i)$ for all cardiac cycles observed for Subject 2. Cardiac cycle percentage is shown on the x-axis, instantaneous heart rate on the y-axis, and velocity magnitude on the z-axis. Velocity is also represented by color according to the color bar on the right. Note that, as expected, the diastolic quiescent period centered at approximately 75% of the cardiac cycle decreases in duration as heart rate increases.

as a function of heart rate and cardiac cycle phase. An example of the interpolated velocity map for Subject 2 is shown in Figure 9, with the blue regions corresponding to minimal velocity and cardiac quiescence. From Figure 9, the systolic and diastolic quiescent periods can be readily identified and the relative durations of these periods with respect to heart rate can be observed.

2.1.1.2 Active Contour Tracking

Active contour tracking is used to validate the frame-to-frame deviation measures in regard to approximating the velocity magnitude of the IVS. Active contour methods provide a flexible framework for feature-based segmentation from image data. Active contour evolution relies both on constraints placed on the shape of the contour by the user and on the image characteristics along the contour. The balance of these two effects is tuned based on application and content of the image or sequence.

Classical active contour methods rely on discretizing the contour as a series of vertices, often referred to as *snaxels*, resulting in a contour $C(p) = \langle x(p), y(p) \rangle$, where

p is the contour length parameterized and normalized to one [48]. The solved contour is found by minimizing the contour energy, expressed as

$$E_{contour} = \int_0^1 (E_{int}(C(p)) + E_{img}(C(p)))dp, \tag{6}$$

where E_{int} is the energy associated with the shape of the contour and E_{img} is the energy associated with the image content along the contour. E_{img} is most often chosen to be a decreasing function of the gradient of the image to attract the contour to edges in the image.

Extending active contour models to a sequence of frames is generally accomplished by finding the contour on a frame-by-frame basis with each frame being solved with knowledge of only the current and previous frame. The solution of the previous frame is used as an estimate for the contour position in the following frame. Different schemes, such as optical flow [49] and Kalman filtering [46], are often employed to improve the estimation of the contour position in the next frame.

Active contours for this work are solved using a method based on [49], where optical flow is calculated according to [50] for the B-mode sequence and used in conjunction with the previous active contour solution to estimate the position of the contour in the subsequent frame. Optical flow attempts to estimate frame-to-frame movement by defining a small neighborhood around each pixel in the current frame and then locating this neighborhood in the following frame.

The cardiac-feature tracking algorithm identifies the feature of interest in each frame of B-mode data. The algorithm is initialized with the user providing an approximate outline consisting of 10 points along the boundary of the cardiac feature in the first frame of the sequence. The rough contour defined by these points is upsampled by five resulting in the evolution of a contour defined by 50 discrete points. The numerical active contour technique presented in [51] is used to find the outline of the feature in each frame by minimizing (6). For all frames after the first, the position of the previous contour, along with optical flow data of the sequence, is used to initialize the active contour algorithm.

Velocity from Active Contour Tracking Knowledge of the velocity magnitude of the cardiac anatomic feature of interest can be used to validate the approximation provided by the frame-to-frame deviation methods described in Section 2.1.1.1. The velocity magnitude can be calculated from the two-dimensional velocity of the feature obtained by differencing the position of the contour in each frame. The position is calculated for each frame by finding the centroid of the cardiac feature, defined as the average location of the pixels inside the contour,

$$\overline{x}(i) = \frac{1}{N}\sum_{x \in S_i} x, \qquad \overline{y}(i) = \frac{1}{N}\sum_{y \in S_i} y, \tag{7}$$

where S_i is the set of all pixel locations inside the contour of frame i and N is number of elements in S_i.

The two-dimensional velocity of the IVS is approximated by taking the first difference of $\overline{x}$ and $\overline{y}$. This process is summarized by

$$\hat{v}^x_{AC}(i) = \overline{x}(i) - \overline{x}(i-1), \qquad \hat{v}^y_{AC}(i) = \overline{y}(i) - \overline{y}(i-1), \tag{8}$$

where $\hat{v}^x_{AC}(i)$ and $\hat{v}^y_{AC}(i)$ are the approximated x and y velocities. The velocity magnitude of the IVS is then defined as

$$\hat{v}_{AC}(i) = \sqrt{\hat{v}^x_{AC}(i)^2 + \hat{v}^y_{AC}(i)^2}. \tag{9}$$

2.1.2 Results of Echocardiography-Based Detection

To assess the efficacy of B-mode detection of cardiac quiescence as well as the characteristics of cardiac quiescent periods for a small healthy population (10 subjects, 23-45 years old) the following results are provided. First, active contour tracking was validated in the direction of ultrasound interrogation using synchronously acquired TDI data. Next, the velocity magnitude of the IVS, $\hat{v}_{echo}(i)$, calculated from the deviation measure was confirmed using the velocity magnitude of the IVS from active contour tracking, $\hat{v}_{AC}(i)$. Then, Bland-Altman analysis was used to compare the quiescent periods indicated by the square regions of the deviation matrix, $\mathbf{D}(i, j)$, and the approximated velocity, $\hat{v}_{echo}(i)$. Lastly, the nature of the quiescent periods for the ten subjects was observed from $\hat{v}_{echo}(i)$.

2.1.2.1 Data Acquisition

For this work, ECG and echocardiographic data were synchronously acquired from 10 human subjects with no known cardiac conditions (4 male, 6 female, 23-45 years) using an Ultrasonix SonixTouch ultrasound machine (Analogic, Peabody, MA, USA). Emory University's Institutional Review Board approved the subject evaluations, and full, written, informed consent was obtained from each subject. The IVS was observed from the apical four-chamber view. For all but the first three subjects, data were recorded in multiple 10-second intervals during breath hold. The first two subject datasets consist of two 30-second intervals recorded pre- and post-exercise without breath hold. This choice was originally made to observe the effect of heart rate on cardiac quiescence. The third subject dataset was acquired during one breath hold. ECG data were acquired at a rate of 200 Hz while B-mode data were acquired at frame rates of either 30 or 50 frames per second (fps).

2.1.2.2 Active Contour Tracking

The IVS was successfully segmented and tracked for seven of the 10 subjects using the active contour algorithm presented in Section 2.1.1.2. For those not tracked, poor acoustic windows, acoustic shadowing, and out of plane motion proved problematic. Tracking was found to show little sensitivity to the initialization of the contour. An example of a solved active contour for a given frame is provided in Figure 10. Here LV and RV are the left and right ventricle, and LA and RA are the left and right atrium. The position of the IVS was found for each frame using the centroid calculation given in (7). From the x- and y-position vectors, the velocity magnitude was calculated

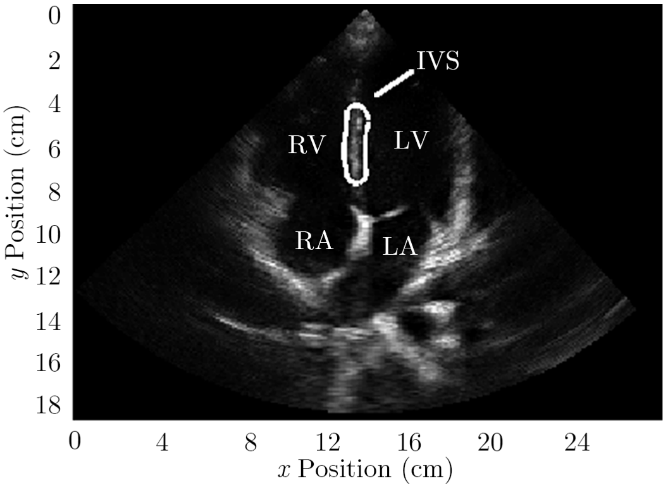

Figure 10: B-mode frame obtained from the apical four-chamber view of heart, with solved contour shown around the IVS. The four chambers: right ventricle (RV), right atrium (RA), left ventricle (LV), and left atrium (LA) are shown.

using first-difference methods as described in (9).

To verify the accuracy of the two-dimensional active contour tracking, the velocity calculated from the active contour centroids was compared to the velocity from synchronously acquired TDI data. As a direct measurement of tissue velocity based on the Doppler shift of the received ultrasonic pulses, TDI is often used to measure the one-dimensional velocity of cardiac features in the direction of ultrasonic interrogation. Active contour based velocity in the direction of ultrasonic interrogation—*axial direction*—was found to agree with that of TDI, indicating that active contours provide accurate velocity information. In addition, the active contour based velocity in the *lateral direction*, orthogonal to the direction of interrogation and not detected by TDI, was found to be significant. This suggests that B-mode derived two-dimensional velocity provides a more complete representation of IVS motion than TDI. An example of these two normalized velocities is shown in Figure 11. Clearly, the magnitude of the TDI velocity will be substantially different than the actual magnitude of the velocity, which is approximated by the velocity derived from active contour tracking.

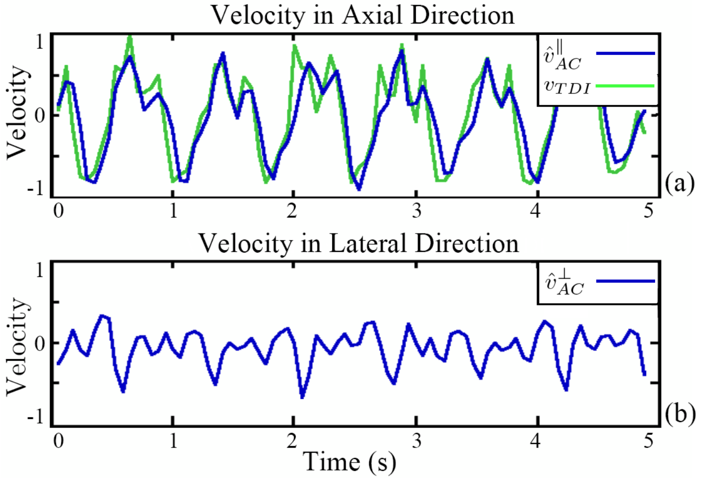

Figure 11: Comparison of the active contour velocity, $\hat{v}_{AC}$, and TDI velocity, v_{TDI}, in blue and green, respectively.

2.1.2.3 Quiescence from Frame-to-Frame Deviation

The deviation matrices, $\mathbf{D}(i,j)$, for each subject were calculated and the velocity of the IVS was approximated by the one-off diagonal, $\mathbf{D}(i,i-1)$, as described in Section 2.1.1.1. Note that frame-to-frame deviation methods could be used for all 10 subjects as opposed to active contour methods that could only be used for seven subjects. To verify the accuracy of the velocity approximation, a number of velocity signals, $\hat{v}_{echo}(i)$ from (5), were compared to the velocity signals derived from active contour tracking, $\hat{v}_{AC}(i)$ from (9). Figure 12 shows an example of this comparison and demonstrates that the velocity derived from the frame-to-frame deviation measure matches that derived from active contour tracking. In addition, the velocity approximation based on deviation was observed to have less noise in the quiescent periods with low velocity magnitude. This is most likely due to noise that is accentuated by the differentiation of digital signals.

Quiescent periods were determined as intervals of the velocity signal, $\hat{v}_{echo}(i)$, less than the mean of $\hat{v}_{echo}(i)$. Quiescence plots, $q(i)$, were then calculated by finding square regions along the diagonal of $\mathbf{D}(i,j)$ with average deviation under a specified

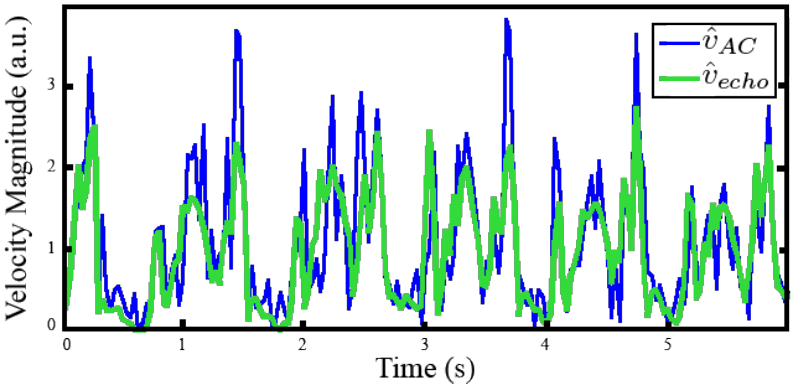

Figure 12: Comparison of the active contour velocity $\hat{v}_{AC}$, and the deviation based velocity $\hat{v}_{echo}$, in blue and green, respectively. Note that the deviation based velocity approximation has less noise in the quiescent periods with low velocity magnitude.

threshold. The mean of $\mathbf{D}$ was used as the threshold for quiescence.

The center and duration of the diastolic quiescent period for each cardiac cycle were then determined for the velocity and corresponding quiescence signals, $\hat{v}_{echo}(i)$ and $q(i)$. For the quiescence signals the peak corresponding to the diastolic quiescent period was found with the position and height indicating the center and duration of the quiescent period, respectively. Both methods for identifying quiescent periods are depicted in Figure 13.

The center and duration of each diastolic quiescent period detected from the velocity and quiescence signals were then compared for all subjects using Bland-Altman analysis to verify agreement between the measurement methods. As shown in Figure 14, the two methods are nearly equivalent in determining quiescence.

Due to the similarity of the velocity and quiescence signals in determining quiescent periods, the velocity signal was chosen to display the analysis of the data due to computational efficiency, requiring only one correlation measure per time index. The nature of quiescent periods can be observed from Figure 15 where the left column of plots indicates all quiescent periods observed longer than 83 ms for four subjects and the right column of plots depicts the interpolated velocity maps of those subjects. The

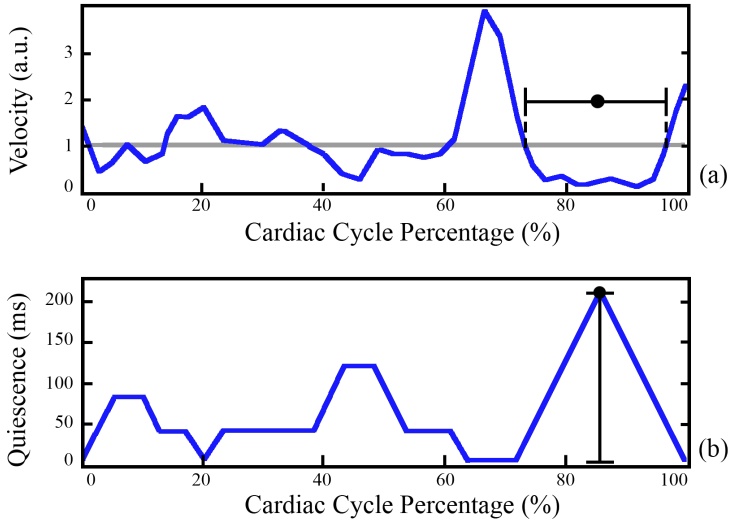

Figure 13: Comparison of diastolic quiescent period detection for the IVS for one cardiac cycle. Quiescent periods can be identified from both the deviation-based velocity signal, $\hat{v}_{echo}(i)$ (a), and the quiescence signal, $q(i)$, computed from square regions of the deviation matrix (b).

cutoff of 83 ms was chosen as it corresponds to the minimum data acquisition time for a dual-source CT machine with a gantry rotation time of 333 ms. As observed in practice, at high heart rates the systolic quiescent period becomes proportionally longer than the diastolic period [52, 53]. This is apparent for Subject 7 in Figure 15 where the duration of the blue region in systole corresponding to minimal velocity becomes longer than that in diastole as heart rate increases.

The diastolic quiescent period statistics for each of the 10 subjects are provided in Table 2. Because the center and duration of the diastolic quiescent periods vary with heart rate, care should be taken in interpreting results for subjects who had a wide range in observed heart rates, indicated by a high heart rate standard deviation. From Table 2, a significant amount of inter- and intra-subject variability can be observed, suggesting that gating based solely on the ECG is suboptimal for predicting the timing of cardiac quiescent periods and that personalized gating protocols could improve this prediction.

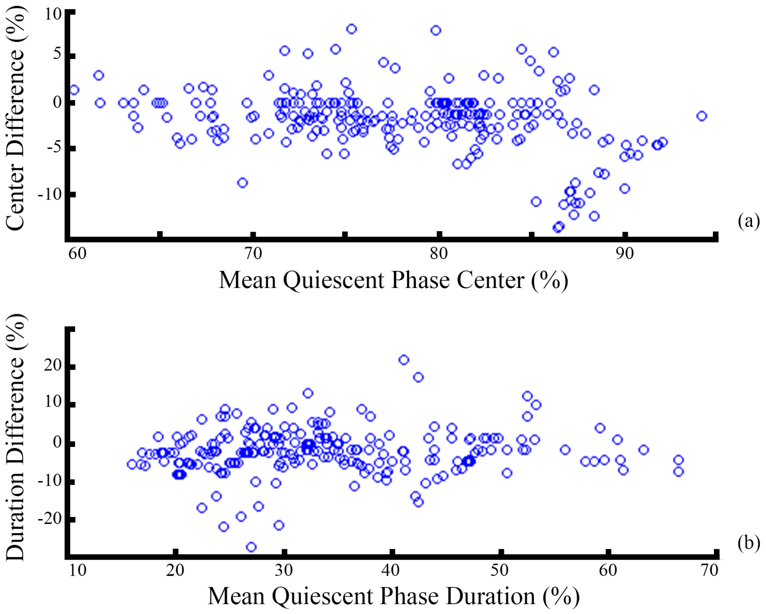

Figure 14: Comparison of diastolic quiescent period identification methods for all cardiac cycles detected from both the velocity signal, $\hat{v}_{echo}(i)$, and the square regions of the deviation matrix. The difference between the two measures is plotted on the vertical axis and the mean of the two measures is plotted on the horizontal axis. The cardiac cycle percent of the period centers (a) and durations (b) are plotted.

2.1.3 Discussion of Echocardiography-Based Detection

Two robust methods for determining cardiac quiescence from B-mode echocardiography were developed. These methods are based on frame-to-frame deviation measures of a user-specified image region and were verified using active contour tracking. The two-dimensional velocity derived from active contour tracking was validated in the axial direction using TDI. In addition, the lateral velocity component, not detected by TDI, was shown to be significant. This suggests that two-dimensional, image-based methods may prove more accurate in determining cardiac quiescence than the more straightforward TDI method of determining myocardial velocity.

These two methods for determining cardiac quiescence were used to analyze data for 10 subjects with no known cardiac conditions. The first method exploits the

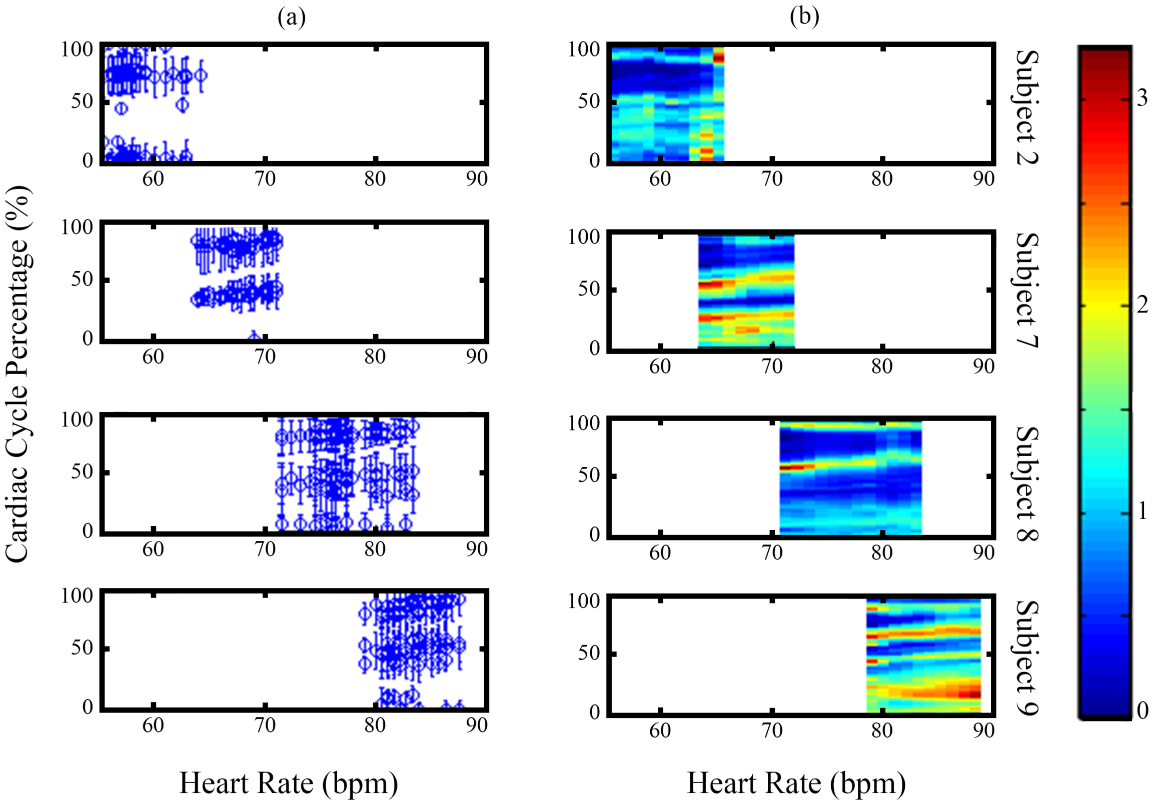

Figure 15: Scatter plots (a) and interpolated velocity color maps (b) shown for four subjects. For the scatter plots, the dots correspond to the quiescent period centers and the bars correspond to the quiescent period durations as determined using the velocity signal, $\hat{v}_{echo}(i)$. For the color maps, blue corresponds to low velocity magnitude and red corresponds to high velocity magnitude.

fact that the correlation between two frames is linearly related to feature displacement, given an assumption of linear motion and feature rigidity between the frames in question as described in Appendix A. The velocity calculated using the deviation of neighboring frames and verified using active contour tracking suggests that, at least for the IVS, these assumptions are reasonable. The second method for determining quiescence from the deviation attempts to identify quiescent periods as square regions of low deviation from the deviation matrix, $\mathbf{D}(i, j)$. Despite using more deviation measures to determine quiescence for each time index, it was observed that this method was actually more susceptible to noise. One possible explanation for

Table 2: Diastolic Quiescent Period Statistics

Subject	Cycles	Heart Rate (bpm)	Period Center (%)	Period Duration (ms)
1	39	58± 5.7	70±4.4	352±113
2	37	58± 2.3	74±1.4	324± 33
3	35	59± 2.3	75±2.4	446± 73
4	61	60±10.7	74±6.4	451±203
5	31	63± 1.5	79±6.6	246±107
6	23	66± 2.9	72±8.1	150± 87
7	39	68± 2.0	84±3.4	301± 80
8	42	77± 2.8	82±2.2	182± 32
9	43	83± 2.1	86±4.8	188± 71
10	10	99± 5.9	75±4.3	203± 40

this is that the deviation measures of a long sequence of frames allow more time for inadvertent transducer, subject, or breathing motion whereas with the velocity approximation technique, only neighboring frames are compared. Despite this, the two methods were found to agree with one another. The proposed deviation-based methods were able to identify quiescent periods for the three subjects where active contour tracking was not possible due to loss of tracking. It is important to note that although quiescent periods can be identified for B-mode sequences with poor imaging, accuracy may be decreased and cannot be verified by active contour tracking. In addition to robustness, these methods provide a less noisy velocity signal than that provided by active contour methods, as active contour tracking requires differentiation to approximate velocity. Lastly, deviation methods are also much more computationally efficient than active contour methods, requiring only correlation measures instead of solving complicated minimization problems and performing optical flow calculations for each B-mode frame. Although not required for the applications in this work, deviation-based velocity calculation could be done in real-time.

The choice of a region-based correlation method was made to provide a robust and efficient technique to determine the magnitude of the velocity of a specified ROI. Speckle tracking is another commonly used method to ascertain motion using optical flow to calculate the frame-to-frame displacement of the pixels inside an ROI [54]. For the application presented in this work, the pixel displacements could be averaged over the ROI to obtain the velocity magnitude of the cardiac feature in the ROI. This could then be used to find quiescent periods. Because pixel-level, two-dimensional motion between frames is estimated, more descriptive motion quantification could be performed. However, speckle tracking is not without drawbacks. It requires high image quality and high B-mode frame rate (60-110 fps), placing substantial constraints on the imaging hardware. To minimize the effect of random noise, speckle tracking is usually averaged over at least three cardiac cycles, making speckle tracking on a beat-by-beat basis problematic. Lastly, speckle tracking is computationally expensive and as a result is generally performed offline after an examination.

Another recent technique for robustly quantifying motion leverages the fact that a translation of an object in the image plane corresponds to a phase shift in the Fourier domain [55]. By taking the two-dimensional Fourier transform of a sequence of images the two-dimensional velocity of the feature can be obtained from the phase shifts. Because this method relies on the Fourier transform and peak detection, it is more computationally expensive than the proposed region-based correlation method.

One potential concern with determining quiescence from the frame-to-frame deviation is that only the relative velocity magnitude is provided. Normalization of the velocity signals partially alleviates this concern because a constant threshold for quiescence can be employed. If needed, absolute velocity magnitude can be obtained either by fitting the deviation-based velocity to a reference velocity, e.g., the velocity from the active contour tracking, as described in Appendix A by (47), (48), and (49), or by leveraging the relationship in (43). The latter method does not require a reference velocity and would rely on how well the relationship between the area of feature overlap between frames and the feature displacement is known.

In light of these results, it is reasonable to suggest that the correlation of neighboring frames can be used to efficiently approximate the magnitude of the velocity of cardiac features, and hence cardiac quiescence. By knowing the precise timing of cardiac quiescent periods, effective methods for quiescence prediction can be developed and analyzed. The periods detected using these methods serve as a baseline to compare periods predicted using CT compatible techniques as described in Chapter 3. Two potential approaches for cardiac-motion-informed gating are offline and real-time methods. Prior to a CTCA exam, offline methods would focus on obtaining patient specific gating parameters for the standard ECG gating that is currently in use. In this case, the proposed echocardiography detection methods could be used directly. Real-time gating involves predicting quiescent periods during the CTCA exam. Therefore, it is necessary for the sensing device used for gating to be CT compatible. Unfortunately, standard echocardiographic transducers are not CT compatible because of the extensive streak artifacts that they would cause in the CT images.

Fortunately, SCG is a CT compatible technique because modern accelerometers are small enough to not interfere with CT acquisition. Therefore, SCG could provide a cardiac-motion-based signal that can be used for predicting cardiac quiescent periods and potentially gating CTCA [56]. For SCG methods for real-time prediction, the proposed echocardiography detection methods are used to assess the predictive accuracy of these methods as described in Section 3.4.1.

2.2 Computed-Tomography-Based Quiescence Detection

Quiescent periods of the cardiac cycle are detected from cardiac CT using a phase-to-phase deviation measure analogous to the frame-to-frame method used in Section 2.1. Quiescence is detected from cardiac CT to establish the relationship between the quiescent periods of the IVS and those of the coronary vessels. It is important that the quiescent periods of the IVS represent those of the vessels because the quiescent periods of the IVS, detected on a beat-by-beat basis from B-mode echocardiography as described in Section 2.1.1.1, are used to assess the performance of the prediction methods provided in Chapter 3.

2.2.1 Methods for CT-Based Detection

For this work cardiac quiescence is estimated from retrospective cardiac CT studies. Reconstructions were obtained at one percent increments from 20% to 80% of the cardiac cycle for 20 subjects. As before, cardiac phase (%) is defined using the R-R interval of the ECG. For each reconstruction, five cardiac features are segmented using a manually-guided, semi-automated approach. The features include the IVS and the left main (LM), left anterior descending (LAD), left circumflex (LCX), and right coronary (RCA) arteries. The IVS is segmented to compare IVS motion to that of the coronary vessels. Using a robust deviation measure based on the phase-to-phase correlation of each of these five cardiac features, the quiescence characteristics of the coronary vessels were investigated.

2.2.1.1 Data Acquisition

Retrospective cardiac CT data were acquired from 20 human subjects (11 male, 9 female, 33-74 years) using a Siemens Somatom Definition dual-source 64-slice CT scanner (Siemens, Erlangen, Germany). These subjects were examined independently of this study for various clinical indications and the data were collected retroactively with the approval of the Emory University Institutional Review Board (IRB). Informed consent requirement was waived by the IRB. CT volume reconstructions were created at one percent increments of the cardiac cycle from 20% to 80% based on the electrocardiogram (ECG) signal used for gating during data acquisition.

2.2.1.2 Segmentation of Cardiac Features

Segmentation of the coronary vessel and IVS features is performed using a semi-automated approach wherein the feature is manually segmented for an undersampled number of axial slices containing the feature, i.e., each manually-segmented slice is separated by several non-manually-segmented slices. The manual segmentations were performed by a graduate researcher under the guidance of a radiologist. The segmentations of the feature for the remaining slices are calculated using an interpolation scheme based on the signed distance function (SDF) of the two neighboring, manually-segmented slices. The final three-dimensional (3D) segmentation is then constructed by combining all of the segmented slices.

The set of pixels defining the location of the feature in a given slice form a set S. The SDF of S is defined as

$$\phi_S(x,y) = \begin{cases} d_S(x,y) & \text{if } (x,y) \in S \\ -d_S(x,y) & \text{if } (x,y) \notin S \end{cases} \tag{10}$$

where $d_S(x,y)$ is the Euclidean distance from the point (x,y) to the nearest point on the boundary of S. It follows that $\phi_S(x,y)$ will be zero on the boundary of S and greater than zero inside S.

The segmentations of the non-manually-segmented slices are interpolated from the SDF of the two nearest-neighboring, manually-segmented slices. Note that the manually-segmented slices may have more than one slice between them. Let $\phi_{S_z}(x,y)$ be the SDF for the axial slice at height z. The slice interpolation scheme is then defined as

$$\phi_{S_z}(x,y) = \frac{(z^+ - z)\phi_{S_{z^-}} + (z - z^-)\phi_{S_{z^+}}}{z^+ - z^-},\ z^- < z < z^+ \tag{11}$$

where z^- and z^+ are the heights of the proximal superior and inferior manually-segmented slices in the craniocaudal direction, respectively. The segmentation for each slice at a height z is then defined as the set of points, (x,y), where $\phi_{S_z}(x,y)$ is greater than or equal to zero, i.e.,

$$\{S_z \in \mathbb{R}^2 : S_z = (x, y),\ \phi_{S_z}(x, y) \geq 0\}. \tag{12}$$

The final 3D segmentation, V, is obtained by combining all of the segmented slices, i.e.,

$$\{V \in \mathbb{R}^3 : V = (x, y, z),\ z_{min} \leq z \leq z_{max},\ (x, y) \in S_z\} \tag{13}$$

where z_{min} and z_{max} are the superior and inferior boundaries of the cardiac feature in the craniocaudal direction.

2.2.1.3 Identification of Intra-Feature Cardiac Quiescenct Periods

Quiescent periods of the coronary vessels and the IVS are calculated using a correlation-based, phase-to-phase deviation measure. In short, the deviation between a segmented feature at a given cardiac phase and neighboring phases is computed. This deviation measure will decrease as the cardiac feature becomes more quiescent.

For this work, the deviation between cardiac phases is expressed as a negative function of the Pearson correlation coefficient taken over the feature volume. This method is a 3D analogue to the method proposed to analyze cardiac quiescence from echocardiography in Section 2.1 and [57]. The Pearson correlation coefficient has been shown to be a strong indicator of image similarity and, as such, can be interpreted as a measure of the similarity of the feature position between two phases [45]. The correlation coefficient between two phases, i and j, is given as

$$\rho_{V_s}(i, j) = \frac{\sum\limits_{(x,y,z)\in V_s} (I_i(x, y, z) - \overline{I}_i^{V_s})(I_j(x, y, z) - \overline{I}_j^{V_s})}{\sqrt{\sum\limits_{(x,y,z)\in V_s} (I_i(x, y, z) - \overline{I}_i^{V_s})^2 \sum\limits_{(x,y,z)\in V_s} (I_j(x, y, z) - \overline{I}_j^{V_s})^2}} \tag{14}$$

where I_i is the imaged volume at phase i, V_s is a static set of voxels containing the feature for all phases, and $\overline{I}_i^{V_s}$ is the mean of I_i in V_s.

Here V_s is chosen to be the union of the segmentations for all phases and is defined as

$$V_s = \bigcup_i V_i \tag{15}$$

where V_i is the set of voxels in $\mathbb{R}^3$ indicating the segmentation for cardiac phase i. This choice of V_s provides the smallest set containing the segmentations of all phases.

The phase-to-phase deviation is calculated as

$$\mathbf{D}(i,j) = 1 - \rho_{V_s}(i,j) \tag{16}$$

for all possible phase-to-phase pairs. The resulting *deviation matrix* for a specific vessel can then be viewed as an image allowing for the quiescent periods to be readily identified visually. An example of $\mathbf{D}(i,j)$ for the LM, LAD, LCX, and RCA of Subject 2 viewed as images is shown in Figure 16 with blue regions along the diagonal corresponding to quiescent periods.

Aggregate Vessel Deviation To investigate the motion of the coronary vessels taken in aggregate for each subject, a deviation matrix is formed from the union of the four static volumes representing the LAD, LM, LCX, and RCA found using (15). That is, the aggregate deviation for all vessels for each subject is defined as

$$\mathbf{D}_{agg}(i,j) = 1 - \rho_{V_{agg}}(i,j) \tag{17}$$

where V_{agg} is the union of all vessel segmentations for a given subject.

Quiescence from Approximated Velocity The velocity magnitude of the vessel in the direction orthogonal to the primary axis of the vessel is approximately proportional to the phase-to-phase deviation. This holds because the value of $\mathbf{D}(i,j)$ is approximately linear with vessel displacement in the orthogonal direction. This approximation holds as long as between phases i and j the vessel is cylindrical, does not deform, moves linearly, and is displaced less than the feature radius. Because the

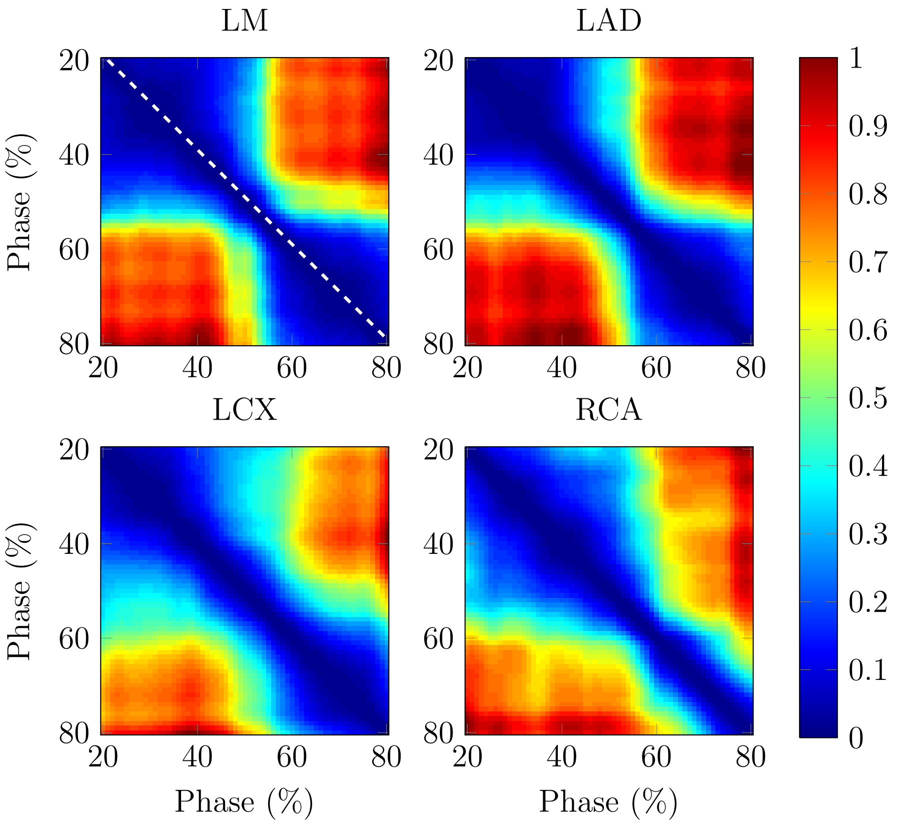

Figure 16: Deviation matrices for the LAD, LM, LCX, and RCA of Subject 2. Blue regions along the diagonal correspond to quiescent periods. The one-off diagonal, $\mathbf{D}(i, i-1)$, is indicated by a dashed white line on the deviation matrix of the LM.

phase delay between neighboring cycles is only one percent, the velocity magnitude can be approximated by the deviation between sequential phases defined as

$$\hat{v}_{CT}(i) = \mathbf{D}(i, i-1) \tag{18}$$

where $\hat{v}_{CT}(i)$ is the approximated velocity of the vessel at phase i, and $\mathbf{D}(i, i-1)$ is the one-off diagonal of the deviation matrix.

For this work, quiescent periods are defined from the velocity approximation as phases of the cardiac cycle when $\hat{v}_{CT}(i)$ is less than the mean of $\hat{v}_{CT}(i)$. This choice was made to ensure that each vessel was thresholded in a comparable manner. An example of this process for the LM of Subject 2 is provided in Figure 17.

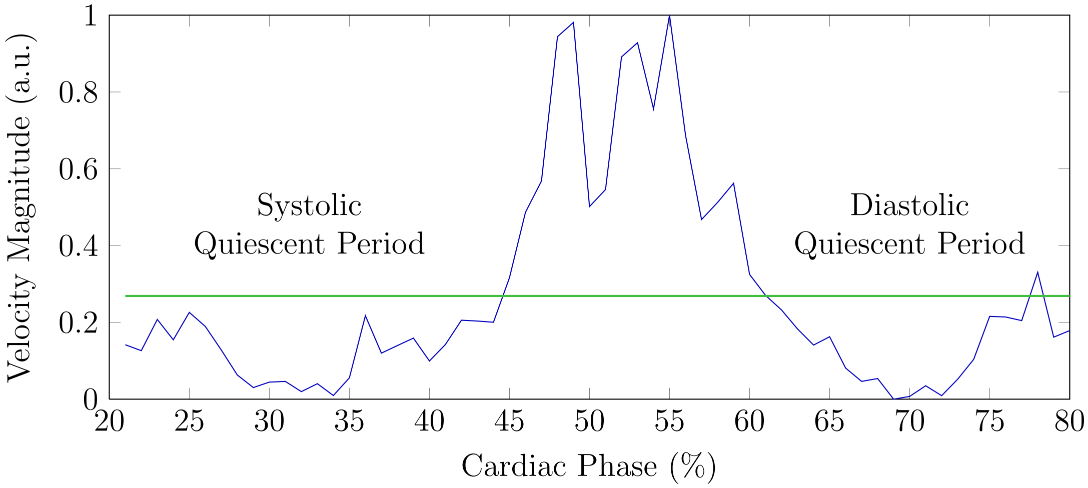

Figure 17: Normalized approximated velocity of the LM for Subject 2 with the systolic and diastolic quiescent periods indicated. The threshold for quiescence is chosen to be the mean of the approximated velocity signal, indicated in the figure by the green line.

Identification of Optimal Quiescent Phases Ideally, the acquisition time of the CT scanner should be taken into account in identifying quiescent phases. This is accomplished by finding the minimum of an averager operating on a square neighborhood sliding along the diagonal of $\mathbf{D}(i,j)$. The mean of the square neighborhood corresponds to the similarity of the consecutive phases that make up the neighborhood. The size of the square neighborhood is chosen to correspond to the data acquisition time of the CT scanner. For this work the acquisition time is 83 ms, corresponding to the quarter gantry rotation time taken by a dual-source CT scanner with a rotation time of 333 ms. As an example, for a subject with a heart rate of 60 bpm, one percent of the cardiac cycle will equal 10 ms. Therefore, a neighborhood covering eight percent will approximately cover the 83 ms necessary for data acquisition. By finding the neighborhood with the minimum mean deviation, the optimal quiescent phase is found. The output of the moving averager, called the *deviation signal*, can be expressed as

$$d(i) = \frac{1}{N^2} \sum_{n_1=-N/2}^{N/2} \sum_{n_2=-N/2}^{N/2} \mathbf{D}(i+n_1, i+n_2), \tag{19}$$

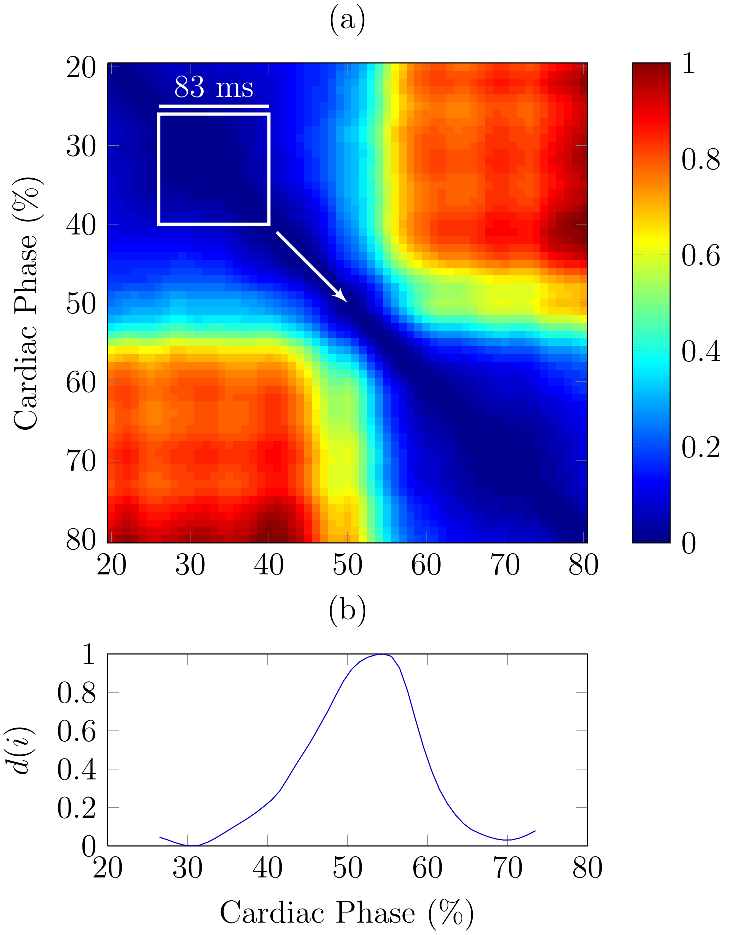

Figure 18: Deviation matrix for the LM of Subject 2 showing the moving averager operating on a square neighborhood with a size corresponing to 83 ms. The normalized output of the moving averager, $d(i)$, is shown in (b).

where N is the width of the neighborhood. A graphical representation of this idea is provided in Figure 18 where the moving averager operating on $\mathbf{D}(i,j)$ and the resulting $d(i)$ are shown for the LM of Subject 2. Note that the deviation signal is a smoothed version of the approximated velocity shown in Figure 17.

2.2.1.4 Diagnostic Quality of Optimal Quiescent Phases

The diagnostic quality of the optimal quiescent phases as determined in Section 2.2.1.3 was compared to that of the quiescent phases predicted by the CT scanner. The optimal quiescent phase was determined for each of the 20 subjects from the aggregate vessel motion. The diagnostic quality of the LM, LAD, LCX, and RCA were graded for both the optimal and predicted quiescent phases by a blinded radiologist with four years experience in interpreting cardiac CT scans. The studies were presented in random order. A paired *t*-test was performed to obtain a preliminary assessment of the validity of the observed difference between the diagnostic quality of the optimal and predicted quiescent phases.

2.2.1.5 Comparison of Inter-Feature Cardiac Quiescence

The similarity of the deviation signals from Section 2.2.1.3 is found using a weighted correlation technique to compare the $d(i)$ for pairs of features. The correlation used is a modification of the the standard Pearson correlation measure that is weighted more heavily in regions where $d(i)$ is smaller, e.g., more quiescent. The weighted correlation is defined as

$$\rho_w(d_x, d_y) = \frac{\sum_n w(n)(d_x(n) - \overline{d}_x)(d_y(n) - \overline{d}_y)}{\sqrt{\sum_n w(n)(d_x(n) - \overline{d}_x)^2 \sum_n w(n)(d_y(n) - \overline{d}_y)^2}} \tag{20}$$

where d_x and d_y are the deviation signals of the two features, w is the weighting vector, and $\overline{d}$ is the weighted mean of d. For this work the weight vector is defined as the normalized distance from the maximum to the minimum of the average of d_x and d_y. This can be expressed as

$$w(i) = \frac{\hat{d}_{max} - \hat{d}(i)}{\hat{d}_{max} - \hat{d}_{min}} \tag{21}$$

where $\hat{d}(i) = (d_x(i) + d_y(i))/2$, and $\hat{d}_{min}$ and $\hat{d}_{max}$ are the minimum and maximum of $\hat{d}(i)$, respectively. This choice of weighting vector results in $w = 0$ when $\hat{d}(i) = \hat{d}_{max}$ and $w = 1$ when $\hat{d}(i) = \hat{d}_{min}$. An example of the deviation signals for the IVS and the aggregate vessel motion are given in Figure 19. The two signals are normalized to have zero mean and unit power, and have a weighted correlation of 0.879.

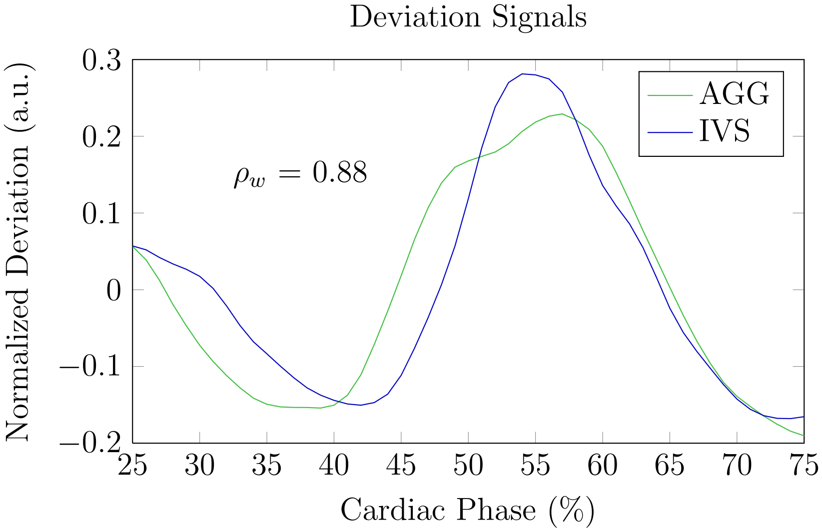

Figure 19: Deviation signals for the IVS and aggregate vessel motion, normalized to have zero mean and unit power. The two signals have a weighted correlation of 0.88 calculated from (20).

2.2.2 Results of CT-Based Detection

The reconstructed CT volumes for 20 subjects were segmented and the motion of the LM, LAD, LCX, RCA, coronary vessels taken in aggregate, and IVS was investigated. The approximated velocity magnitude of each of the cardiac features was found and used to identify the center and duration of the quiescent periods of each feature. The optimal quiescent phase for each feature was found using the method described in Section 2.2.1.3. Lastly, the deviation signal comparison technique described in Section 2.2.1.5 was used to determine if the IVS is a suitable predictor of aggregate vessel quiescence.

2.2.2.1 Segmentation of the Coronary Vessels and Interventricular Septum

The LM, LAD, LCX, RCA, and IVS were segmented using the approach outlined in 2.2.1.2. The average ratio of total number of segmented slices to the number of manually-segmented slices was three and eight for the coronary vessels and IVS, respectively. These ratios indicate the overall segmentation speed-up achieved by using the proposed method, rather than manually segmenting each slice.

2.2.2.2 Center and Duration of Quiescent Periods

The center and duration of the systolic and diastolic quiescent periods of the LM, LAD, LCX, RCA, coronary vessels taken in aggregate, and IVS were calculated using the method described in 2.2.1.3. The systolic quiescent period was defined as the longest quiescent period with a center occurring before 60% of the cardiac cycle as defined by the R-R interval of the ECG. The diastolic quiescent period was defined in the same manner but with a center occurring at or later than 60%. The results of these calculations are shown in Figure 20 where the systolic and diastolic quiescent periods for each subject are plotted against the heart rate of the subject.

From Figure 20, the position and duration of the quiescent periods exhibit a large amount of inter-subject variability. This suggests that the ECG alone may be suboptimal in terms of predictive accuracy of cardiac quiescence.

The subjects were separated into low (below 65 bpm), medium (from 65 to 85 bpm), and high (above 85 bpm) heart rate ranges. There were six subjects with low heart rates, six with medium heart rates, and eight with high heart rates. The tabulated results of each vessel for each range are provided in Table 3.

From Figure 20 and Table 3, the duration of the systolic periods in terms of percent of the cardiac cycle can be seen to increase with heart rate, while that of the diastolic periods can be seen to decrease with heart rate. This agrees with the accepted standard that at higher heart rates cardiac imaging data should be obtained during systole [20].

2.2.2.3 Optimal Quiescent Phases

The optimal quiescent phase of each cardiac feature was found for each of the 20 subjects. This was accomplished by determining the minimum of the deviation signal $d(i)$ as defined in (19). In addition, the optimal quiescent phase of the vessels taken in

Table 3: Quiescent Period Statistics

HR	Feature	Systolic Periods		Diastolic Periods	
		Center (%)	Duration (ms)	Center (%)	Duration (ms)
Low					
(< 65 bpm)	LM	36.2±4.1	151.8±47.3	73.9±2.7	212.5±56.6
	LAD	35.2±2.1	182.9±50.0	73.2±3.3	197.4±78.2
	LCX	38.1±5.5	171.6±61.4	74.0±4.1	210.8±81.3
	RCA	39.7±4.9	146.3±44.4	75.1±1.1	192.0±27.3
	AGG	39.4±4.7	160.9±77.4	74.7±3.1	200.7±62.1
	IVS	36.1±1.5	137.7±35.1	74.4±1.4	205.0±29.8
Medium					
(65–85 bpm)	LM	43.6±3.4	139.0±46.5	76.7±2.0	145.9±34.2
	LAD	38.9±3.6	144.4±59.2	76.6±2.4	146.8±39.9
	LCX	43.7±2.3	132.6±39.1	75.6±1.4	159.1±24.3
	RCA	42.4±3.9	181.6±53.0	78.0±1.0	118.7±25.4
	AGG	41.7±2.3	151.2±33.3	77.2±0.8	135.8±19.2
	IVS	40.9±5.1	138.0±33.6	76.8±1.3	143.3±18.0
High					
(> 85 bpm)	LM	44.8±4.3	149.0±34.3	74.7±4.2	49.1±36.8
	LAD	43.6±6.3	151.6±43.0	76.5±4.5	42.4±28.4
	LCX	43.8±6.7	146.3±55.8	77.4±5.5	47.8±43.0
	RCA	44.1±4.9	163.5±36.8	76.9±5.4	44.4±37.7
	AGG	45.1±5.0	165.0±35.8	76.1±5.1	42.0±45.4
	IVS	42.5±6.1	122.3±39.1	80.7±4.5	61.5±58.4

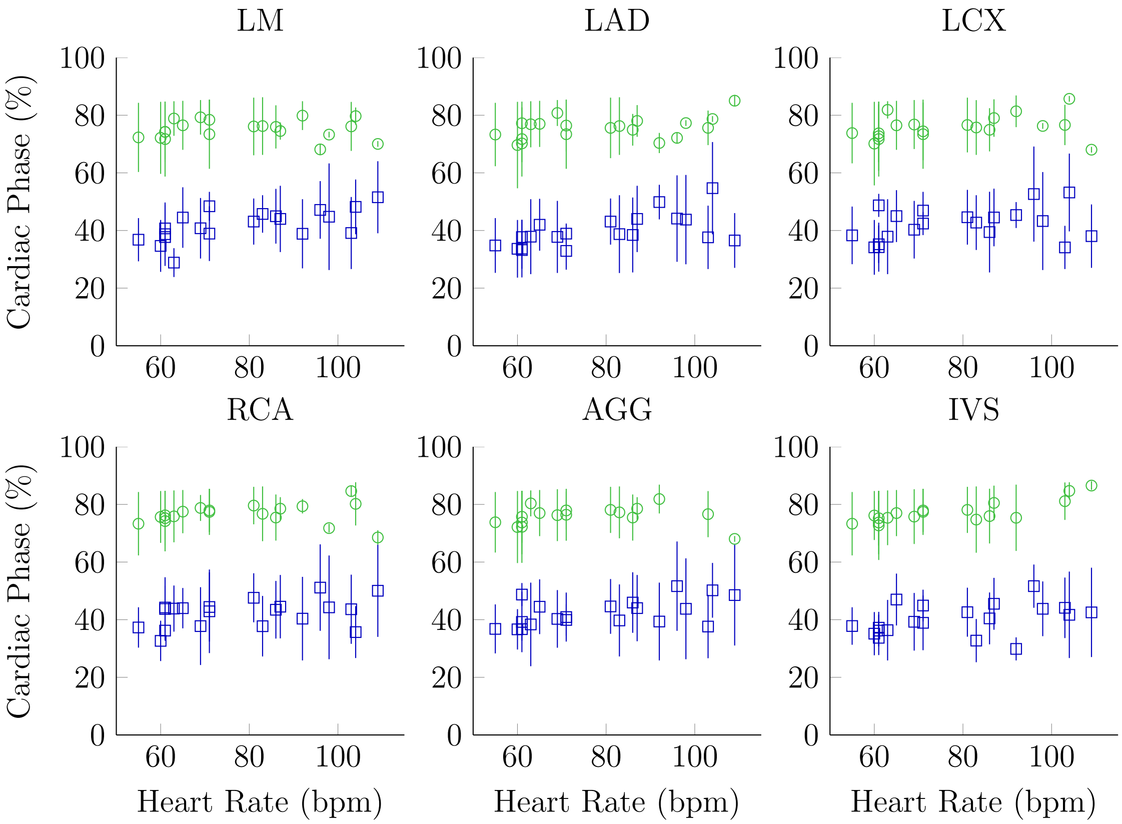

Figure 20: Quiescent periods of the LM, LAD, LCX, RCA, coronary vessels in aggregate, and IVS for each of the 20 subjects. Systolic quiescent periods are blue and diastolic quiescent periods are green. The centers of the quiescent periods are indicated by the marker and the durations by the length of the lines extending from the period centers. Note that not every subject had both a systolic and diastolic quiescent period.

aggregate was computed from the aggregate deviation matrix as defined in (17). The subjects were separated into low, medium, and high heart rate ranges, as before. A summary of the statistics is provided in Table 4. Note that a high standard deviation for a given heart rate range corresponds to some optimal phases being in systole and some in diastole. This is most apparent for medium heart rates (from 65 to 85 bpm) because the optimal phase transitions from diastole to systole in this heart rate range.

An interesting conclusion that can be drawn from Table 4 is that the optimal quiescent phase of the RCA transitions to systole at a lower heart rate than the other

Table 4: Optimal Quiescent Phase Statistics (%)

Feature	Low HR (< 65 bpm)	Medium HR (65–85 bpm)	High HR (> 85 bpm)
LM	78.2± 1.7	67.5±15.4	45.3± 5.3
LAD	76.9± 2.7	71.8±14.8	43.9± 6.7
LCX	71.7±13.3	71.8±13.8	45.9± 9.6
RCA	71.6±12.3	51.0±13.2	46.6± 5.9
AGG	71.7±15.9	72.7±13.6	45.9± 3.0
IVS	79.1± 1.8	79.8± 1.5	59.0±16.2

vessels and that the optimal phase of the IVS transitions to systole at a higher heart rate than the coronary vessels. Also of note is that the optimal quiescent phase of the vessels when taken in aggregate is very similar to each individual vessel with the exception of the RCA.

2.2.2.4 Inter-Feature Comparison of Deviation Signals

The deviation signals for each cardiac feature were compared for all subjects using the weighted correlation technique described in Section 2.2.1.5. In addition to comparing each feature to every other feature, the IVS was compared to the aggregate deviation signal representing all vessels. This comparison was performed to observe the similarity of the deviation signal of the IVS to the coronary vessels taken as a whole. Prior to calculating the weighted correlation, all signals were normalized to have zero mean and unit power. The summary of the comparison is presented in Table 5 with the subjects separated into low, medium, and high heart rate ranges as described in Section 2.2.2.2. An example of two deviation signals with a weighted correlation of 0.83 is provided in Figure 19.

The similarity of the deviation signals tends to decrease as heart rate increases, with the deviation signals of subjects with low heart rates being very similar. In addition, the IVS tends to be more similar to the deviation signal representing aggregate vessel motion than the deviation signals representing each individual vessel. This suggests that the IVS is a better predictor for aggregate vessel motion than for

Table 5: Average Correlations of Deviation Signals

Low Heart Rate (< 65 bpm)

	LM	LAD	LCX	RCA	AGG	IVS
LM	1.00	0.92	0.89	0.82	0.91	0.87
LAD	—	1.00	0.85	0.79	0.85	0.83
LCX	—	—	1.00	0.76	0.91	0.82
RCA	—	—	—	1.00	0.86	0.82
AGG	—	—	—	—	1.00	0.84
IVS	—	—	—	—	—	1.00

Medium Heart Rate (65–85 bpm)

Med. HR	LM	LAD	LCX	RCA	AGG	IVS
LM	1.00	0.83	0.91	0.76	0.90	0.77
LAD	—	1.00	0.87	0.61	0.84	0.78
LCX	—	—	1.00	0.73	0.92	0.76
RCA	—	—	—	1.00	0.85	0.67
AGG	—	—	—	—	1.00	0.81
IVS	—	—	—	—	—	1.00

High Heart Rate (> 85 bpm)

High HR	LM	LAD	LCX	RCA	AGG	IVS
LM	1.00	0.65	0.75	0.68	0.86	0.63
LAD	—	1.00	0.72	0.51	0.67	0.53
LCX	—	—	1.00	0.59	0.79	0.78
RCA	—	—	—	1.00	0.86	0.57
AGG	—	—	—	—	1.00	0.64
IVS	—	—	—	—	—	1.00

Dashes represent symmetric entries about the diagonal.

specific vessel motion. The deviation signal of the IVS is least similar to that of the RCA.

2.2.2.5 Comparison of Optimal Quiescent Phases to those Predicted by the CT Scanner

The optimal quiescent phase of the coronary vessels when taken in aggregate was compared to the nearest systolic or diastolic quiescent phase predicted from the ECG by the CT scanner for each subject. The results of this comparison are shown in Figure 21. The average absolute difference in terms of phase is 5.1% suggesting that

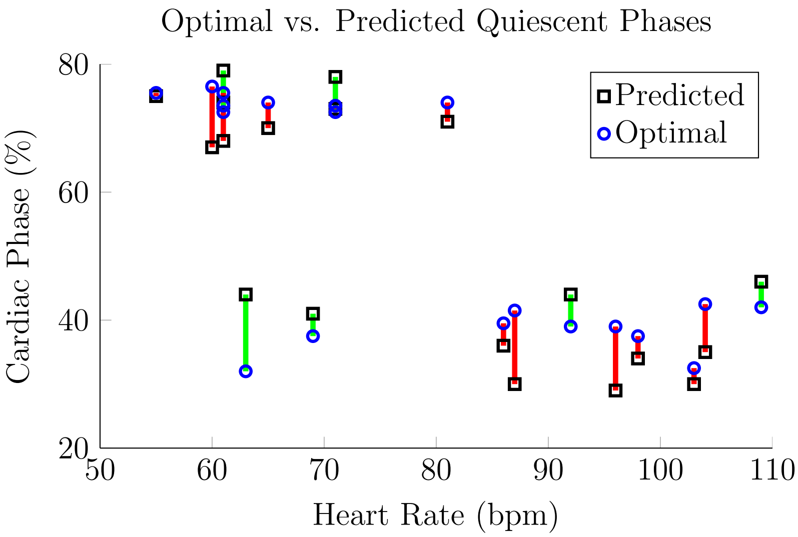

Figure 21: Comparison of the phase predicted by the CT machine to the calculated optimal quiescent phases of the aggregate vessel motion for each subject. Optimal and predicted phases are indicated by blue circles and black squares, respectively. The line connecting the optimal and predicted phases is red if the predicted phase occurs before the optimal phase and green otherwise.

the ECG-based method used for predicting quiescence is not optimal. Figure 21 also shows that there is no bias toward under- or over-prediction and that the predicted phases are more variable than the actual optimal phases.

To quantify the effect that this error in prediction by the CT scanner has on diagnostic quality, the CT volumes corresponding to each of the optimal and predicted phases (40 in total) were read by a practicing radiologist. The diagnostic quality of the LM, LAD, LCX, and RCA was graded on a scale from one (excellent) to four (non-diagnostic). The average diagnostic quality grade along with the paired *t*-test values for each segment are given in Table 6. In general, the phases calculated according to the method presented in Section 2.2.1.3 were of higher diagnostic quality than those predicted by the CT machine. This improvement was most pronounced for the right coronary artery (RCA). The diagnostic quality of the RCA improved for 10 studies by using the calculated optimal phase instead of the CT scanner predicted phase. Conversely, only one study became worse. An example of a study that went from

Table 6: Mean Diagnostic Quality Grades and p-values for Each Coronary Vessel

	Optimal	Predicted	p-value
LM	1.4	1.3	0.577
LAD	2.2	2.1	0.577
LCX	2.5	2.7	0.297
RCA	2.3	2.9	0.004

One — excellent, four — non-diagnostic.

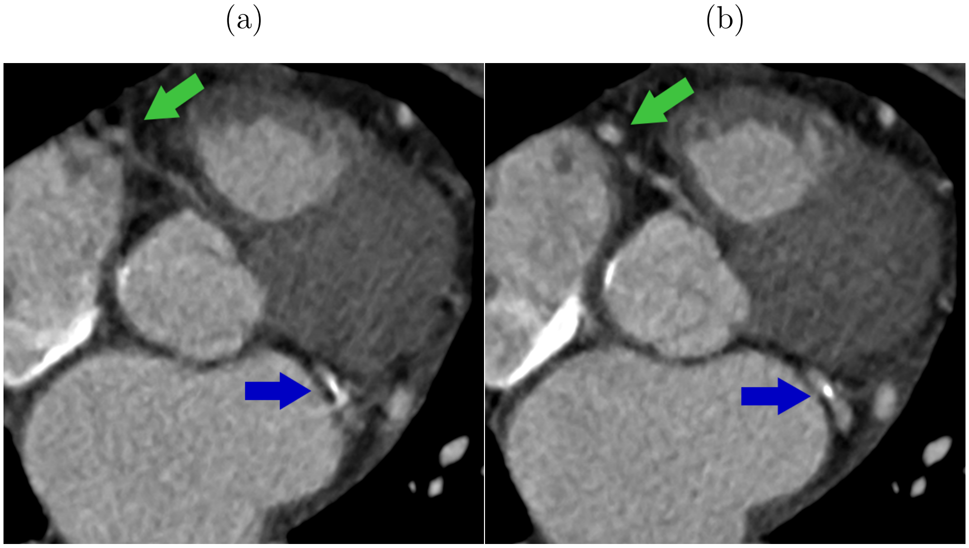

Figure 22: Comparison of the diagnostic quality of the RCA and LCX for the CT scanner predicted quiescent phase (a) and calculated optimal quiescent phase (b). The RCA is indicated by a green arrow and the LCX is indicated by a blue arrow.

non-diagnostic to diagnostic for both the LCX and RCA is shown in Figure 22.

2.2.2.6 Discussion of CT-Based Detection

To better understand cardiac quiescence, a novel method for robustly quantifying the cardiac quiescence of specific cardiac features from cardiac CT reconstructions was developed. This method is based on a deviation measure calculated from the phase-to-phase correlation of each cardiac feature. Understanding cardiac quiescence is critical to the performance of many cardiac imaging modalities, including CTCA, that rely on acquiring imaging data while the heart is relatively stationary.

To analyze the quiescence of the coronary vessels and IVS, a novel semi-automated method was developed to segment each cardiac feature. An undersampled number of axial slices were manually segmented. The segmentations for the missing slices were then interpolated from the neighboring manually-segmented slices. When compared to manually segmenting each slice, this approach resulted in an average speed-up by a factor of three for the coronary vessels and eight for the IVS. A semi-automated approach to segmentation was needed because reconstructions containing motion artifacts would prove problematic for a completely automated approach. In general, when automated vessel segmentation is attempted it is performed at pre-determined phases that are free from motion artifacts [58].

The coronary vessels and the IVS were investigated for 20 patients. The systolic and diastolic quiescent periods were found to be similar across cardiac features. The statistics of the quiescent periods showed a dependency on subject heart rate. This was most notable for the duration of the diastolic quiescent period, which was much shorter for high heart rates (above 85 bpm). As can be seen from Table 3, the longest quiescent phase transitions from diastole to systole as heart rate increases. This is in line with the accepted consensus that the optimal gating window occurs in diastole for low heart rates and systole for high heart rates [16, 53].

The optimal quiescent phase of each coronary vessel, the vessels taken in aggregate, and the IVS were detected by finding the most quiescent period with a length of 83 ms. This duration corresponds to the minimum acquisition time of the CT scanner used for this work. The optimal quiescent phase of the RCA was found to transition from diastole to systole at a lower heart rate than the other coronary vessels. On the other hand, the optimal quiescent phase of the IVS was found to transition at a higher heart rate than the coronary vessels.

Advanced CT reconstruction methods are another approach to improving image quality in the presence of motion [40, 59]. Even when using these techniques it is still prudent to avoid as much motion during acquisition as possible. Thus, the results and methods presented in this work can supplement advanced reconstruction techniques.

For each subject, the coronary vessels, the vessels taken in aggregate, and the IVS were compared to observe the overall motion similarity among the different cardiac features. The similarity between the features was high for low heart rates and decreased as heart rate increased. The motion of the IVS was found to be more similar to the aggregate vessel motion than the motion of individual vessels, suggesting that the IVS is a better predictor of aggregate vessel motion than for specific vessel motion.

To assess the accuracy of the quiescent phases predicted by the CT scanner, the optimal quiescent phase of the coronary vessels taken in aggregate were compared against the predicted best phase by the CT scanner for each subject. The predicted phases were found to differ from the optimal phases by an average of 5.1% in terms of absolute phase difference. Also, the difference between the optimal and predicted quiescent phases showed no positive or negative bias and did not trend with heart rate. Taken together, this suggests that there is room for improvement in predicting cardiac quiescence for the purpose of gating cardiac CT acquisition.

The IVS was found to be a suitable predictor of vessel quiescence, especially for aggregate vessel quiescence. Aggregate vessel quiescence is most important in terms of cardiac imaging, as it is typically desired to diagnose all coronary vessels from one exam. Liu *et al.* showed that the IVS was an accurate predictor of LAD vessel quiescence [44]. From Table 5, the LAD is in fact among the least similar to the IVS, suggesting that if the IVS is a suitable predictor for the LAD it will be as good or better for the other vessels. The quiescence of the IVS is of particular interest because it can be readily observed using echocardiography, as opposed to the coronary vessels. The use of echocardiography to analyze cardiac quiescence is extremely useful because it is a real-time visualization of cardiac state. By verifying the relationship between the IVS and the coronary vessels, echocardiography can be used to analyze cardiac quiescence on a beat-by-beat basis [57].

A limitation of this work is that the CT reconstructions used only covered the range of 20%–80% of the cardiac cycle. This range of the cardiac cycle was chosen because it has been shown to contain the optimal systolic and diastolic quiescent phases [52, 60]. However, since the remainder of the cardiac cycle, i.e., between 80% and 20% is not reconstructed, it is possible that the start of the systolic or end of the diastolic quiescent period may lie outside the 20%–80% reconstructed interval of the cardiac cycle. This is apparent in Figure 20, where a number of quiescent periods begin either at 20% or end at 80%. This may explain the difference between the phase of the quiescent period centers and the optimal quiescent phases. An artificially truncated quiescent period will be biased away from the boundaries of the reconstructed interval. This is because each quiescent period center is defined as the midpoint between the beginning and end of that quiescent period. On the other hand, the method used to find the optimal quiescent phase is independent of the beginning and end phase of the quiescent period.

Lastly, by observing motion directly from CT reconstructions, beat-to-beat heart rate variability is not taken into account. This is because the CT reconstructions are created from data acquired over multiple cardiac cycles. Observing intra-subject variability is important to understand how it affects diagnostic quality. It has been shown that as heart rate variability increases the diagnostic image quality decreases [61]. For this reason, it is also important to observe quiescence on a beat-by-beat basis, suggesting that echocardiography and other signals derived directly from cardiac motion will be complementary in the analysis and prediction of cardiac quiescence.

A robust approach for identifying and analyzing cardiac quiescence from retrospective cardiac CT scans was developed. The center and duration of the quiescent periods were found and the optimal quiescent phases were computed for each subject. The predicted best reconstruction phases by the CT scanner were found to differ from the optimal quiescent phases by 5% in terms of absolute phase. The method used to compute the optimal phase could potentially be used by the CT scanner to accurately determine the best phase to reconstruct for retrospective cardiac exams. Lastly, the IVS was found to be a suitable predictor of vessel quiescence, suggesting the applicability of echocardiography as a tool for observing quiescence on a beat-by-beat basis.

2.3 Seismocardiography-Based Quiescence Detection

As a direct indication of chest wall acceleration due to cardiac motion, SCG can be used as an indication of cardiac quiescence [56, 62, 63]. Cardiac quiescence is determined from periods of minimal velocity magnitude derived from the SCG signal. Though SCG is a one-dimensional representation of cardiac motion, it is CT compatible and can be used for the real-time prediction of cardiac quiescence. Therefore, SCG has strong potential to supplement ECG as a signal for cardiac gating of imaging data acquisition.

2.3.1 Methods for SCG-Based Detection

Cardiac quiescence is detected from SCG on a beat-by-beat basis and from composite velocity signals. A Kalman filter is used to obtain a robust estimate of the chest wall velocity in real-time from the SCG. The magnitude of this velocity is then estimated using a sliding window root mean square (RMS) technique. From the velocity magnitude, quiescence is detected on a beat-by-beat basis. Lastly, to obtain a more robust indication of velocity magnitude on average as a function of heart rate, the observed cardiac cycles are sorted by their instantaneous heart rates and averaged to form composite signals. Quiescent periods are then calculated from these composite signals.

2.3.1.1 Beat-by-Beat Detection of Cardiac Quiescence from SCG

Cardiac quiescence is detected from the SCG as periods of minimal velocity by using a Kalman filter to calculate the chest wall velocity from the acceleration provided by the SCG. The Kalman filter framework provides a robust method for estimating the underlying true acceleration and velocity from the potentially noisy SCG [64, 65]. As with echocardiography and CT, quiescence will be defined as periods of minimal velocity.

Velocity is estimated in real-time from the acceleration signal provided by the SCG, $a(i)$, using a constant-jerk Kalman filter formulation. The model state is defined as

$$\mathbf{x}(i) = \begin{bmatrix} x(i) \\ v(i) \\ a(i) \\ j(i) \end{bmatrix}, \tag{22}$$

where $x(i)$ is the position, $v(i)$ is the velocity, $a(i)$ is the acceleration, and $j(i)$ is the jerk of the SCG accelerometer sensor. The update equations can then be defined as

$$x(i) = x(i-1) + v(i-1)\Delta t + a(i-1)\frac{\Delta t^2}{2} + j(i-1)\frac{\Delta t^3}{6}, \tag{23a}$$

$$v(i) = v(i-1) + a(i-1)\Delta t + j(i-1)\frac{\Delta t^2}{2}, \tag{23b}$$

$$a(i) = a(i-1) + j(i-1)\Delta t, \tag{23c}$$

$$j(i) = j(i-1), \tag{23d}$$

where Δt is the sampling period. By introducing jerk into the model, the accuracy of $a(i)$ will increase because the assumption of constant acceleration between samples is no longer necessary. Though (23d) indicates that jerk is constant, this is not the case. The resulting model error in the jerk term can be accommodated by setting the process error associated with the jerk term equal to the expected variance of the jerk.

The Kalman update equation for this model is defined as

$$\mathbf{x}(i) = \mathbf{A}\mathbf{x}(i-1) + \mathbf{w}, \tag{24}$$

where $\mathbf{A}$ is the state transition matrix and $\mathbf{w}$ is the process error. Next, the observation equation is defined as

$$\mathbf{z}(i) = \mathbf{H}\mathbf{x}(i) + \mathbf{v}, \tag{25}$$

where $\mathbf{z}(i)$ is the observation, $\mathbf{H}$ is the measurement matrix, and $\mathbf{v}$ is the measurement noise at time index i.

The update equations, defined by (23), result in a state-transition matrix of

$$\mathbf{A} = \begin{bmatrix} 1 & \Delta t & \frac{\Delta t^2}{2} & \frac{\Delta t^3}{6} \\ 0 & 1 & \Delta t & \frac{\Delta t^2}{2} \\ 0 & 0 & 1 & \Delta t \\ 0 & 0 & 0 & 1 \end{bmatrix}. \tag{26}$$

The jerk term of the process error, $\mathbf{w}$, will be equal to the variance of dj/dt. This variance is approximated by computing the variance of $a(i+1) - 2a(i) + a(i-1)$.

Because only acceleration is measured by the SCG, the measurement matrix will be

$$\mathbf{H} = \begin{bmatrix} 0 & 0 & 1 & 0 \end{bmatrix}, \tag{27}$$

and the measurement error, $\mathbf{v}$, will be equal to the variance of the signal noise in $a(i)$.

The velocity of the chest wall, $v_{SCG}(i)$, is calculated from the SCG using a combination of low-pass, notch, and Kalman filters. The SCG is first low-pass filtered with a cutoff of 20 Hz to remove higher frequency content associated with the sounds of the cardiac valves. The resulting signal is then notch filtered to remove any DC offset and respiratory motion. The resulting signal, $a(i)$, is then passed through a Kalman filter to obtain a robust estimation of the chest wall velocity, $v(i)$. The velocity is then passed through an additional notch filter to remove any lingering DC bias. This process is summarized by the block diagram shown in Figure 23.

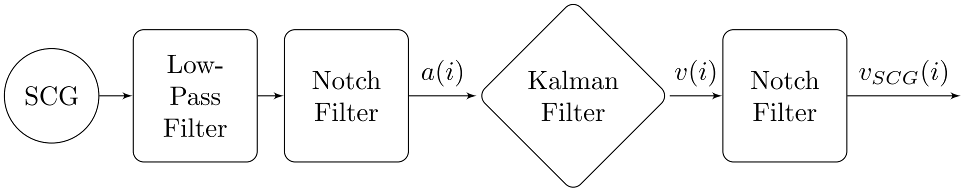

Figure 23: Signal processing flow to determine chest wall velocity from the SCG.

The approximate magnitude of the chest wall velocity, $\hat{v}_{SCG}(i)$, is calculated as the windowed RMS of $v_{SCG}(i)$. An 83 ms rectangular window is used for two reasons. First, the resulting signal will be a smoothed version of the velocity magnitude of the chest wall making identification of quiescent periods easier. Second, an 83 ms window corresponds to the typical data acquisition time of a dual-source CT scanner. Each value of $\hat{v}_{SCG}(i)$ corresponds to the RMS of the chest wall velocity for a length of time corresponding to the CT data acquisition time centered at i. The windowed RMS is calculated as

$$\hat{v}_{SCG}(i) = \sqrt{\frac{1}{N}\sum_{n=-N/2}^{N/2} v_{SCG}^2(i+n)}, \tag{28}$$

where N is is the number of samples corresponding to 83 ms. An example of $v_{SCG}(i)$ and $\hat{v}_{SCG}(i)$ along with the synchronized ECG are shown in Figure 24. Quiescent periods are determined as time intervals where $\hat{v}_{SCG}(i)$ is less than the mean of $\hat{v}_{SCG}$ for each cardiac cycle as defined by the synchronously acquired ECG.

2.3.1.2 Quiescence from Composite Velocity Signals

To identify the overall nature of cardiac quiescence from the SCG for a range of observed heart rates, composite velocity magnitude signals are generated for each subject. These composite signals are created by segmenting the velocity magnitude signal, $\hat{v}_{SCG}(i)$, by the R-R interval of the synchronously recorded ECG signal. After segmentation, the instantaneous heart rate for each cycle is derived from the known cycle length in seconds. Cycles of the velocity magnitude signal can then be sorted

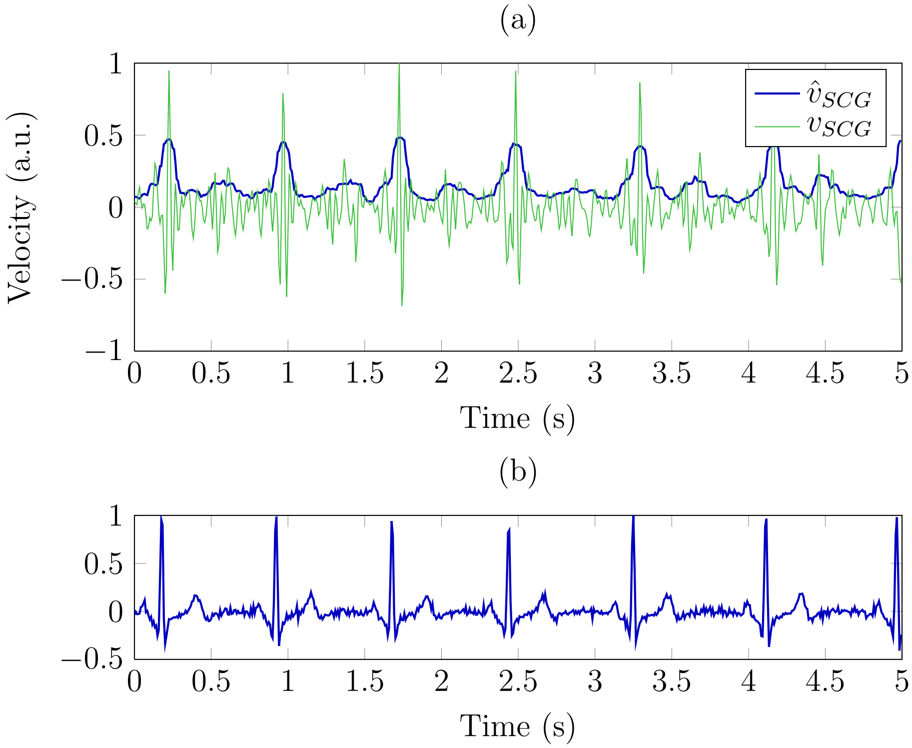

Figure 24: Plot of chest wall velocity, v_{SCG}, and velocity magnitude, $\hat{v}_{SCG}$, from the SCG (a) along with the synchronized ECG (b).

into groups by the instantaneous heart rate of each cycle. After sorting, the segmented cycles are time-scaled to equal length, allowing the groups to be averaged and compared. This process is summarized as

$$\overline{v}_m(i) = \frac{1}{N_m} \sum_{\hat{v}_n \in H_m} \hat{v}_n(i), \tag{29}$$

where $\overline{v}_m(i)$ is the composite velocity magnitude signal for heart rate range H_m, N_m is the number of cycles in the range H_m, and $\hat{v}_n(i)$ is the n^{th} time-scaled velocity magnitude cycle in H_m. Quiescent periods can be determined from each $\overline{v}_m(i)$ providing cardiac quiescence information as a function of instantaneous heart rate for each subject. Similar to beat-by-beat detection presented in Section 2.3.1.1, quiescent periods are detected as time intervals when $\overline{v}_m(i)$ is less that the mean of $\overline{v}_m(i)$.

2.3.2 Results of SCG-Based Detection

Quiescent periods were detected from the SCG for nine healthy human subjects. For each subject, the systolic and diastolic quiescent periods were identified on a beat-by-beat basis. Composite velocity magnitude signals were then computed across the range of observed heart rates. Lastly, composite velocity maps and the corresponding quiescent periods were generated for each subject.

2.3.2.1 Data Acquisition

SCG and ECG data were synchronously acquired for nine healthy human subjects at a rate of 1.2 kHz using the custom SCG acquisition device described in Section 1.4.1. Full informed consent was obtained from each subject in accordance with the Emory University Institutional Review Board. Two of the subjects were examined solely for the SCG. The SCG of the remaining seven subjects was acquired continuously while the patient received an echocardiogram used in Section 2.1.

2.3.2.2 Detection of Quiescent Periods

The systolic and diastolic quiescent periods were identified for each cardiac cycle using the methods presented in Section 2.3.1.1. As with echo and CT, the systolic quiescent period was defined as the longest quiescent period with a center occurring before 60% of the cardiac cycle as defined by the R-R interval of the ECG. The diastolic quiescent period was defined in the same manner but with a center occurring at or later than 60%. A summary of the identified quiescent periods is provided in Table 7. From Table 7, the duration of the diastolic periods in terms of ms can be seen to decrease with heart rate, while that of the systolic periods is relatively independent of heart rate. Note that the subject numbers are consistent between Table 7 and Table 2 from Section 2.1.2.3.

In addition to beat-by-beat detection, quiescent periods were identified for composite velocity magnitude signals using the methods of Section 2.3.1.2. For each

Table 7: Quiescent Period Statistics

Subject	Cycles	Heart Rate	Systolic Periods		Diastolic Periods	
			Center (%)	Duration (ms)	Center (%)	Duration (ms)
4	210	49.6±5.0	22.0± 2.1	161± 8	71.3±2.8	543± 81
11	91	52.0±3.2	24.6± 1.3	132±24	69.5±1.5	639± 50
2	3820	63.9±5.4	30.8±12.8	162±83	76.6±9.2	281±135
7	3801	67.1±6.3	29.5± 6.7	183±54	77.4±6.5	348±114
3	3509	68.4±8.6	30.9± 9.7	187±80	75.9±8.9	322±158
6	3041	74.1±6.5	31.7± 7.5	135±54	75.5±6.3	324±106
8	6445	81.5±6.8	30.8± 6.3	191±54	76.2±6.3	263± 91
9	4481	84.7±3.4	31.1±10.7	129±50	80.8±4.5	236± 56
10	1759	90.1±5.1	32.7± 4.5	173±44	77.9±4.7	227± 62

subject, composite velocity magnitude signals, $\overline{v}_m(i)$ from (29), were generated for heart rate range sets with a width of two beats per minute and 50% overlap at one beat per minute increments. All $\overline{v}_m(i)$ were normalized to have a maximum of one. A composite velocity map of all $\overline{v}_m(i)$ for Subject 8 is provided in Figure 25 with the image intensity corresponding to the velocity magnitude. Quiescent periods were identified for each $\overline{v}_m(i)$ and are indicated on the image in white. Each composite signal represents the average of all velocity magnitude segments with an instantaneous heart rate within ±1 bpm of the rate indicated. From Figure 25, the duration of the period of minimal velocity during mid-diastole decreases as heart rate increases, whereas the duration of the period of minimal velocity during end-systole increases minimally as heart rate increases.

2.3.3 Discussion of SCG-Based Detection

The two methods presented above attack the problem of quiescent period detection from two different angles. The beat-by-beat detection method presented in Section 2.3.1.1 is an approach that can be used to detect quiescence in real-time. The downside to this approach is that it is subject to sensor noise and subject movement. The composite signal method for detecting quiescent periods presented in Section 2.3.1.2 relies on generating typical velocity magnitude signals for the range of heart rates observed for each patient. Because this method relies on averaging many

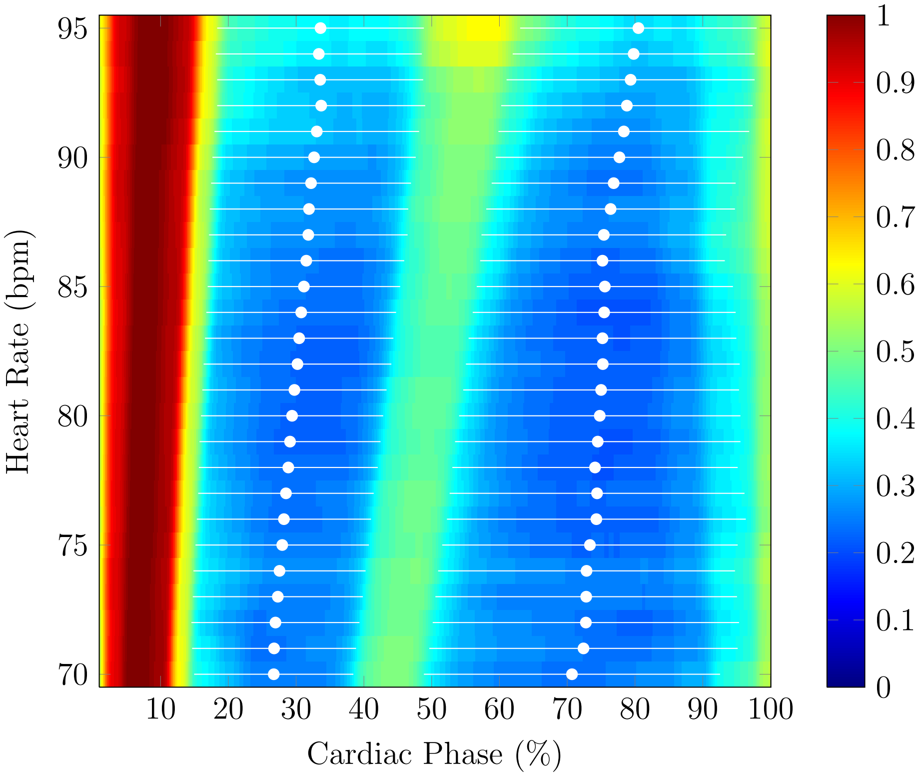

Figure 25: Image of composite velocity magnitudes, $\overline{v}_m(i)$, across a range of heart rates for one subject. The longest systolic (left) and diastolic (right) quiescent periods are indicated in white. The center of each quiescent period is indicated by a white circle and the duration is indicated by the line passing through that circle.

signals together it is more robust at the expense of not being sensitive to beat-by-beat variation in the motion of the chest wall.

Beat-by-beat detection can be used to observe quiescence in real-time with minimal delay. Though this method is sensitive to patient movement, the expected level of patient movement during a CT exam should be similar to that observed for Subject 4 and 11 who were examined solely for the SCG. The results for the remaining subjects demonstrate more noise in terms of standard deviation. It is assumed that this is a result of patient motion due to the simultaneous echocardiography exam each of those subjects received. From Table 7, the amount of noise apparent from the standard deviations of the measurements is much less for Subjects 4 and 11. In addition, the residual of the Kalman filter could be used to estimate the noise of the SCG measurement. Because beat-by-beat detection can identify quiescence in real-time, it serves as an important component of quiescent period prediction from the SCG as described in Section 3.4.1.

Composite velocity magnitude signals can be used to robustly detect the average quiescent periods for the range of heart rates observed for each patient. This approach provides a convenient method for determining the optimal quiescent periods on average according to the SCG at the expense of not being representative of quiescence on a beat-by-beat basis.

2.4 Comparison of Quiescence Detection Methods

The periods of quiescence detected by echocardiography are compared to those detected by SCG for patients who received a synchronous exam. This comparison is made to determine the bias in the periods predicted by the SCG. The center of each detected systolic and diastolic quiescent period are used to estimate the underlying nominal quiescent phases as a function of heart rate for both the echocardiography and SCG. The quiescent period centers are represented in terms of cardiac cycle percentage resulting in a linear relationship between quiescent phase center and heart rate. A linear fit is calculated from the quiescent phase centers for both echocardiography and SCG detected periods as a function of heart rate as shown in Figure 26. The difference between the systolic and diastolic linear fits, defined as P_Δ and shown in Figure 27, represents the bias between echocardiography- and SCG-detected quiescent periods. The quiescent phases from SCG occur before those of echocardiography. Two possible explanations for this exist. First, SCG is a one dimensional measurement and will not be sensitive to some of the motion present observed using echocardiography. Second, the SCG is a measurement of the velocity at the chest wall due to cardiac motion. Thus, some amount of cardiac motion may not be observed at the

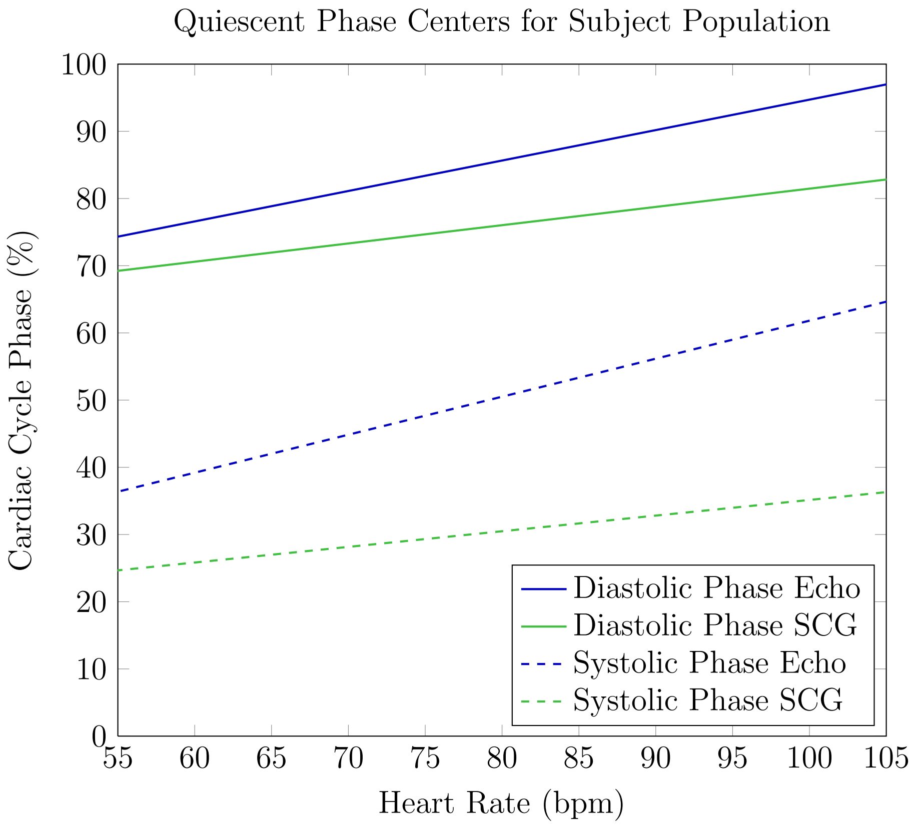

Figure 26: Plot comparing the nominal quiscent period centers detected by echocardiography and SCG.

periphery of the chest wall.

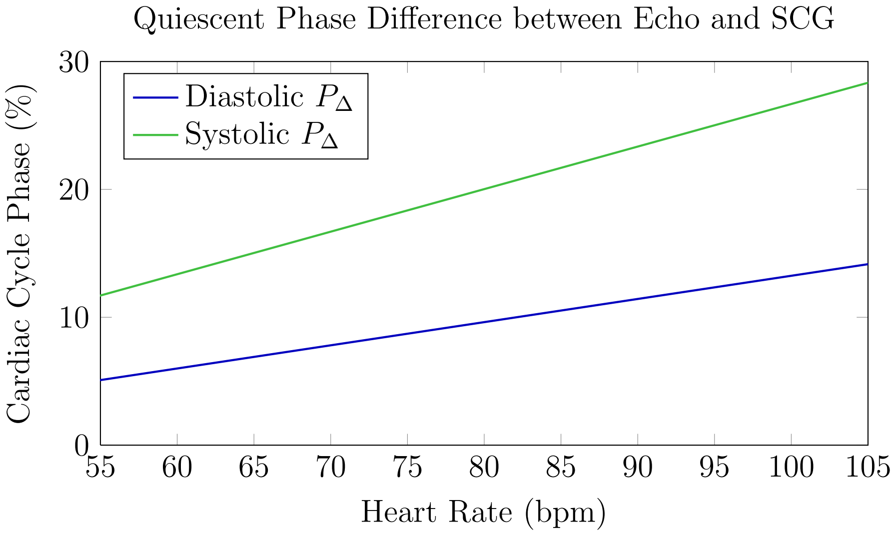

Figure 27: Plot of the difference between echocardiography and SCG detected quiescent period centers.

CHAPTER III

PREDICTION OF CARDIAC QUIESCENCE

The echocardiography- and SCG-based quiescence detection methods outlined in Chapter 2 are used to investigate methods for predicting cardiac quiescence. Quiescent periods of the cardiac cycle can be predicted either using an offline or real-time approach. Offline methods for prediction focus on determining patient-specific CTCA gating parameters that could be obtained prior to a CTCA examination. Once these parameters are obtained, prospective CTCA can then be performed using these parameters translated to the ECG signal. On the other hand, real-time methods for prediction focus on calculating and updating these parameters in real time with the intent of replacing or supplementing ECG-triggered acquisition in the future. Both offline and real-time methods for prediction are compared to the current standard ECG-based prediction for CTCA gating.

3.1 Methods for Assessing Predictive Performance

To quantify the performance of the prediction methods to be presented, it is important to maintain a consistent methodology for assessing each method. As mentioned in Section 2.1, B-mode echocardiography will serve as the baseline for comparing the prediction methods because it provides a beat-by-beat representation of two-dimensional cardiac motion. Each predicted quiescent phase will have an associated temporal and deviation error. The details of the calculation of these errors are provided below.

3.1.1 The Deviation Signal

To represent the cardiac motion that would take place during CT data acquisition, a moving averager with a length corresponding to the time needed for CT data acquisition is used. Similar to finding the optimal quiescent phase for CT as described in Section 2.2.1.3, this is implemented with an averager operating on a square neighborhood sliding along the diagonal of the deviation matrix, $\mathbf{D}(i,j)$. The size of the square neighborhood is chosen to be 83 ms, corresponding to one quarter of the gantry rotation time taken by a dual-source CT scanner with a rotation time of 333 ms. The mean of the square neighborhood corresponds to the average displacement of the IVS over the 83 ms duration associated with the size of the averager. The output of the moving averager, called the *deviation signal*, can be expressed as

$$d_{echo}(i) = \frac{1}{N^2} \sum_{n_1=-N/2}^{N/2} \sum_{n_2=-N/2}^{N/2} \mathbf{D}(i+n_1, i+n_2), \tag{30}$$

where N is the width of the neighborhood. A graphical representation of this idea is provided by Figure 28 where the moving averager operating on $\mathbf{D}(i,j)$ and the resulting $d_{echo}(i)$ are shown for three cardiac cycles of B-mode data. Note that the deviation signal is a smoothed version of the velocity approximation, $\hat{v}_{echo}(i)$, and that this method is completely analogous to the method presented for CT detection in Section 2.2.1.3.

3.1.2 Calculation of Prediction Errors

Errors in the prediction of cardiac quiescence will be calculated in terms of time and deviation. The use of time is straightforward because, in general, CT image quality will degrade as the timing error increases. However, sensitivity to mistiming is not constant and depends on the relative duration of quiescence compared to the time needed for CT data acquisition. This is generally a function of heart rate but also varies between individuals. For this reason, errors in prediction will also be quantified using the deviation signal described in Section 3.1.1. By comparing the deviation of the baseline quiescent phase to that of the predicted quiescent phase, the added motion as a result of mistimed prediction can be quantified. This should provide a more accurate indication of the potential degradation in CT image quality than solely observing the error in timing.

The prediction temporal error, e_t, will be calculated as the difference in time between the baseline and predicted quiescent phase as

$$e_t = \hat{t}_q - t_q, \tag{31}$$

where t_q and $\hat{t}_q$ are the timings of the baseline and predicted quiescent phases, respectively. The baseline timing is chosen to be the quiescent period center detected for each cycle from B-mode echocardiography as described in Section 2.1.1.1.

The prediction deviation error, e_d, will be calculated as the difference in deviation between the baseline and predicted quiescent phase as

$$e_d = d_{echo}(\hat{t}_q) - d_{echo}(t_q). \tag{32}$$

Because d_{echo} is normalized to have a minimum of zero and a mean of one, the value of e_d will be represented in terms of scaled distance from the minimum observed deviation ($e_d = 0$) to the mean observed deviation ($e_d = 1$).

Lastly, to observe any relationship between heart rate variability and the temporal error or deviation error, the prediction error for instantaneous heart rate will be calculated as

$$e_r = \hat{r} - r, \tag{33}$$

where $\hat{r}$ is the predicted cycle length and r is the actual cycle length. The prediction error of heart rate will increase as heart rate variability increases.

3.2 Predicting Cardiac Quiescence from the ECG

The ECG is the current standard for predicting cardiac quiescent phases for CTCA acquisition [20]. The predicted phase for ECG is determined by delaying CTCA acquisition from the R-peak of the ECG by an amount of time dependent on the estimated length of the cycle. This estimated length, $\hat{T}$, is determined by observing the cycle length for a small number of preceding cycles, three for this work. The delay amount is generally given as a percentage, P, of the estimated cycle length. The prediction of the quiescent period center is defined by

$$\hat{t}_q = P_{ECG}(\hat{r}) \cdot \hat{T}, \tag{34}$$

where $\hat{r}$ is the estimated instantaneous heart rate and $\hat{t}_q$ is the estimated timing of the quiescent period center relative to the preceding R-peak of the ECG. P_{ECG} is a function of heart rate and is generally defined for heart rate ranges. The suggested values of P generally place $\hat{t}_q$ in diastole for heart rates lower than 80 bpm and in systole for rates 80 bpm or higher [16, 31, 53, 66]. For this work, the optimal phases suggested by [66] will be used for ECG prediction, so P is defined as follows

$$P_{ECG}(\hat{r}) = \begin{cases} 74\% & \hat{r} \leq 60 \text{ bpm} \\ 79\% & 60 \text{ bpm} < \hat{r} \leq 70 \text{ bpm} \\ 80\% & 70 \text{ bpm} < \hat{r} \leq 80 \text{ bpm} \\ 46\% & \hat{r} > 80 \text{ bpm}, \end{cases} \tag{35}$$

where the estimated heart rate, $\hat{r}$, is directly computed from the estimated cycle length, $\hat{T}$, as $\hat{r} = 60/\hat{T}$. These phases agree with the CT quiescence detection results of Section 2.2

3.2.1 Results of ECG-Based Prediction

Quiescent periods were predicted using ECG for the seven subjects in Section 2.3 who received a synchronous echocardiography and SCG exam. This choice was made so

Table 8: Prediction Error for ECG-Based Gating

Subject	Heart Rate (bpm)	e_t (%)	e_d	e_r (bpm)
2	58±2.3	$-$ 3.4± 3.0	0.10±0.14	1.2±1.4
3	59±2.3	$-$ 3.7± 2.1	0.02±0.07	1.7±2.1
6	66±2.9	16.5±20.3	0.68±0.44	1.7±2.0
7	68±2.0	$-$10.4±33.7	0.26±0.34	1.1±1.3
8	77±2.8	$-$34.3±28.7	0.52±0.56	3.3±4.2
9	83±2.1	$-$35.7±17.2	0.46±0.29	1.6±1.8
10	99±5.9	$-$11.6±27.7	0.12±0.32	5.1±6.6

that ECG prediction can be compared to each of the proposed gating techniques to follow.

The results of ECG-based prediction are provided in Table 8. The average and standard deviation of the time, deviation, and heart rate prediction error are given as e_t, e_d, and e_r, respectively, for each subject. These terms are defined in Section 3.1.2.

3.3 Offline Techniques for Predicting Cardiac Quiescence

The most straightforward realization of CTCA gating based on cardiac motion is to perform a preliminary patient exam to identify personalized gating parameters. Quiescence can vary among individuals [47], suggesting that a patient-specific gating protocol will result in more accurate gating performance and subsequently better image quality.

By performing a preliminary echocardiography or SCG exam, gating parameters tailored to each patient can be obtained that would indicate the center of the longest quiescent interval relative to the ECG R-peak for the heart rates observed during the preliminary exam. These parameters can then be used for CTCA to improve standard ECG-based gating. Because this method relies on the ECG R-peak as a trigger, it would still suffer from the sensitivity to high heart rate variability associated with standard ECG gating.

Gating parameters can be obtained using the detection methods in Chapter 2 and represent an average quiescent period for a given heart rate. Gating parameters determined from a simulated preliminary exam using a synchronous cardiac-motion-based and ECG subject dataset are used to predict quiescence for a second dataset. The process is then reversed and quiescence is predicted for the first dataset. The predicted quiescent phases are compared to the actual quiescent phases, as determined by the synchronously acquired B-mode echocardiography, for each cardiac cycle, as shown in Figure 29. This comparison facilitates the estimation of offline prediction performance. To assess the prediction improvement over the current standard, quiescent phases will be compared to those predicted using standard ECG-based methods on a beat-by-beat basis. In addition, offline gating parameters for all subjects are compared, providing information on inter-subject variability of the timing of average quiescent phases.

3.3.1 Echocardiography for Offline Prediction

Quiescence is predicted from patient specific gating parameters calculated for each subject. The data for each subject is split into two datasets and gating parameters are determined from each set. The parameters for each set are then used to predict quiescent phases for the other set.

Gating parameters are obtained during a simulated preliminary examination by first detecting the systolic and diastolic quiescent period centers and durations in terms of cardiac cycle percentage. By using a cardiac cycle percentage representation, the period centers and durations are linearized with respect to heart rate. A linear fit is then performed for both the center and duration of the diastolic and systolic quiescent periods, providing a nominal period center and duration as a function of heart rate. The final gating parameters are defined for each heart rate as the center of the longer of the systolic and diastolic quiescent periods.

Cardiac gating is simulated in much the same way as ECG-based prediction from

Section 3.2. That is, the prediction of the quiescent period center is defined by

$$\hat{t}_q = P_{echo}(\hat{r}) \cdot \hat{T}, \tag{36}$$

where $\hat{r}$ is the estimated instantaneous heart rate and $\hat{t}_q$ is the estimated timing of the quiescent period center relative to the preceding R-peak of the ECG. The estimated heart rate, $\hat{r}$, is directly computed from the estimated cycle length, $\hat{T}$, as $\hat{r} = 60/\hat{T}$. $P_{echo}(r)$ represents the predicted phase as a function of heart rate, i.e., the gating parameters.

3.3.1.1 Results of Offline Echocardiograpahy-Based Prediction

Quiescent periods were predicted using gating parameters obtained from a simulated echocardiography preliminary exam for the seven subjects from Section 2.3 who received a synchronous echocardiography and SCG exam. This choice was made so that the results can be compared to each of the gating techniques proposed in this work.

The results of offline echocardiography-based prediction are provided in Table 9. The average and standard deviation of the time, deviation, and heart rate prediction error are given as e_t, e_d, and e_r, respectively, for each subject. These terms are defined in Section 3.1.2. For Subject 10, a negative deviation error is possible because the minimum deviation may not occur precisely in the center of the periods detected from echocardiography. Therefore, the deviation of the predicted phase can be less than the deviation of the quiescent period center.

3.3.2 Seismocardiography for Offline Prediciton

As shown in Section 2.3, the RMS of the velocity magnitude calculated from SCG can be used to detect cardiac quiescent periods. The prediction methods based on a preliminary SCG exam mirror those given for echocardiography provided in Section 3.3.1 with the exception of an additional quiescent phase mapping step based

Table 9: Prediction Error for Offline Echocardiography-Based Gating

Subject	Heart Rate (bpm)	e_t (%)	e_d	e_r (bpm)
2	58±2.3	$-$ 1.6± 2.1	0.05±0.10	1.2±1.4
3	59±2.3	$-$ 2.5± 1.7	0.01±0.05	1.7±2.1
6	66±2.9	$-$ 2.5±14.3	0.29±0.38	1.7±2.0
7	68±2.0	$-$ 2.6±30.7	0.10±0.23	1.1±1.3
8	77±2.8	$-$ 4.0±26.2	0.13±0.26	3.3±4.2
9	83±2.1	$-$ 1.2±24.3	0.20±0.32	1.6±1.8
10	99±5.9	$-$18.5±27.7	$-$0.05±0.27	5.1±6.6

on the quiescent phase relationship between SCG and echocardiography, observed in Section 2.4. The phase mapping step is utilized to accommodate the consistent bias observed between SCG and echocardiography detected quiescent periods. This bias is calculated for the entire subject population as a function of heart rate. The phase dependent offset is then added to preliminary gating parameters calculated from SCG. This process is summarized as

$$P_{SCG}(\hat{r}) = \tilde{P}_{SCG}(\hat{r}) + P_{\Delta}(\hat{r}), \tag{37}$$

where P_{SCG} is the final SCG-based gating parameters, $\hat{r}$ is the predicted heart rate, $\tilde{P}_{SCG}$ represents the preliminary gating parameters obtained from the SCG in the same manner as echocardiography, and P_{Δ} is the phase mapping function from Section 2.4. The quiescent period center is then predicted as

$$\hat{t}_q = P_{SCG}(\hat{r}) \cdot \hat{T}, \tag{38}$$

where $\hat{t}_q$ is the estimated timing of the quiescent period center relative to the preceding R-peak of the ECG. $P_{SCG}(r)$ represents the predicted phase as a function of heart rate, i.e., the gating parameters.

3.3.2.1 Results of Offline Seismocardiography-Based Prediction

Quiescent periods were predicted using gating parameters obtained from a simulated preliminary SCG exam for the seven subjects from Section 2.3 who received a synchronous echocardiography and SCG exam. This choice was made so that the results

Table 10: Prediction Error for Offline SCG-Based Gating

Subject	Heart Rate (bpm)	e_t (%)	e_d	e_r (bpm)
2	58±2.3	− 4.0± 3.7	0.12±0.14	1.2±1.4
3	59±2.3	− 6.3± 1.2	0.03±0.07	1.7±2.1
6	66±2.9	21.1± 8.2	0.53±0.44	1.7±2.0
7	68±2.0	7.5±17.7	0.10±0.21	1.1±1.3
8	77±2.8	22.9±19.9	0.11±0.41	3.3±4.2
9	83±2.1	7.7±16.2	0.10±0.20	1.6±1.8
10	99±5.9	24.4±33.3	0.48±0.63	5.1±6.6

can be compared to each of the gating techniques proposed in this work.

The results of offline SCG-based prediction are provided in Table 11. The mean and standard deviation of the time, deviation, and heart rate prediction error are given as e_t, e_d, and e_r, respectively, for each subject. These terms are defined in Section 3.1.2.

3.3.3 Discussion of Offline Methods for Prediction

Both echocardiography- and SCG-based offline methods for predicting quiescence performed better than the standard ECG-based prediction for CTCA. This suggests that by obtaining patient-specific gating parameters from either a preliminary echocardiography or SCG exam, the imaging performance of CTCA could be improved. The echocardiography-based method performed better than the SCG-based method. This is expected as a two-dimensional direct representation of the IVS position, the IVS velocity approximated from echocardiography is more indicative of the actual velocity than SCG. Although echocardiography predicted quiescence more accurately than SCG, conducting an SCG preliminary examination could still be desirable. SCG data is much easier to acquire than echocardiography data as it requires no operator involvement after the initial placement of the accelerometer sensor. In addition, SCG acquisition hardware is much less expensive than an ultrasound machine. Thus, both echocardiography and SCG show promise as modalities for obtaining patient specific gating parameters for CTCA.

3.4 Real-Time Prediction of Cardiac Quiescence

Real-time prediction methods are used to update gating parameters on a cycle-by-cycle basis to more accurately predict cardiac quiescence during a CTCA exam. The gating parameters for each cycle are computed from a buffer containing SCG-based, quiescence information for a small number of preceding cycles. SCG is used for real-time prediction because it is a CT-compatible modality that does not require human operator input during acquisition. SCG-based real-time prediction of cardiac quiescence could allow for cardiac-motion-based gating for CTCA, supplementing the ECG R-peak with motion information and a fixed delay with an adaptive one based on actual cardiac quiescence. The overall prediction simulation and analysis framework is provided in Figure 30.

Quiescence is detected in simulated real time by first calculating the mean quiescent period centers for the cycles in the signal buffer. These quiescent phases are detected relative to the ECG as described in Section 2.3. For this work, the buffer contains SCG and ECG data for the previous 30 cardiac cycles. A 30 cycle buffer was observed to balance the noise attenuation characteristics of a longer buffer with the adaptability of a shorter buffer. As in Section 3.3.2, a phase mapping step is included in the prediction. The phase mapping adjusts the mean quiescent periods based on the quiescent phase relationship between SCG and echocardiography, observed in Section 2.4. This real-time prediction process for each cycle is then defined as

$$P_{RT}(\hat{r}) = \bar{P}_{SCG} + P_{\Delta}(\hat{r}), \tag{39}$$

where P_{RT} is the predicted phase, $\hat{r}$ is the predicted heart rate, $\bar{P}_{SCG}$ is the mean quiescent phase of the 30 cycle buffer, and P_{Δ} is the phase mapping function from Section 2.4. The quiescent period center is then predicted as

$$\hat{t}_q = P_{RT}(\hat{r}) \cdot \hat{T}, \tag{40}$$

Table 11: Prediction Error for Real-Time SCG-Based Gating

Subject	Heart Rate (bpm)	e_t (%)	e_d	e_r (bpm)
2	58±2.3	-2.4 ± 3.1	0.00±0.09	1.2±1.4
3	59±2.3	-4.4 ± 3.0	0.03±0.06	1.7±2.1
6	66±2.9	23.9± 5.8	0.87±0.31	1.7±2.0
7	68±2.0	6.2±19.3	0.10±0.22	1.1±1.3
8	77±2.8	23.8±19.9	0.14±0.46	3.3±4.2
9	83±2.1	8.0±16.0	0.10±0.19	1.6±1.8
10	99±5.9	34.3±26.9	0.14±0.34	5.1±6.6

where $\hat{t}_q$ is the estimated timing of the quiescent period center relative to the preceding R-peak of the ECG.

3.4.1 Results of Real-Time Prediciton

Quiescent periods were predicted using gating parameters obtained from a simulated real-time SCG exam for the seven subjects from Section 2.3 who received a synchronous echocardiography and SCG exam. This choice was made so that the results can be compared to each of the gating techniques proposed in this work.

The results of real-time, SCG-based prediction are provided in Table 11. The mean and standard deviation of the time, deviation, and heart rate prediction error are given as e_t, e_d, and e_r, respectively, for each subject. These terms are defined in Section 3.1.2. For Subject 2, a deviation error of zero is possible because the minimum deviation may not occur precisely in the center of the periods detected from echocardiography. Therefore, the deviation of the predicted phase can be less than the deviation of the quiescent period center, resulting in an average e_d of zero.

3.4.2 Discussion of Real-Time Prediction

Real-time SCG-based prediction of cardiac quiescence performed almost the same as the offline SCG-based method for prediction given in Section 3.3.2. This is promising because it implies that a preliminary SCG exam is not necessary and that gating parameters can be calculated during a CTCA exam given an interface between the

Table 12: Comparison of Performance for Each Prediction Method

Method	e_t (%)	e_d
ECG	16.5±19.0	0.31±0.31
Offline Echo	4.7±18.1	0.12±0.13
Offline SCG	13.4±14.5	0.21±0.30
Real-time SCG	14.7±13.4	0.20±0.24

SCG and CT hardware exists.

It should be noted that the proposed method for real-time prediction still relies on the ECG R-peak as a trigger. Ideally, the ECG would be used only as a robust signal to segment cardiac cycles of SCG data. Features of signals derived from the SCG data would then be used to trigger CTCA data acquisition. Cycle-by-cycle feature detection would be a preferred method, but was not implemented for this work due to noise in the SCG signal. This noise has two sources. The first is from patient movement. In general, the cycles making up the buffer correspond to the time period before echocardiography acquisition. During this time there is a high probability of patient motion related to the echocardiography exam. The second source of noise is sensor noise from the acquisition hardware. For some patients, the power of the SCG signal can approach that of the sensor noise. Cycle-by-cycle feature detection could be further explored with improved hardware and SCG data acquired from patients receiving only a SCG exam. The downside to this approach is that without synchronously acquired echocardiography data, there is no way to assess the predictive performance of these methods.

3.5 Comparison of Prediction Methods

The average absolute value of the prediction errors for each of the prediction methods is given in Table 12, where e_t and e_d are the time and deviation prediction error, respectively. In addition, the average standard deviation of each of the error terms is also given.

From Table 12, offline echocardiography-based prediction performs the best, both in terms of time and deviation error. This is expected for two reasons. First, echocardiography is used for the baseline of comparison. Gating parameters calculated from echocardiography will inherently be better than SCG at predicting quiescence as determined from echocardiography. Second, the velocity approximated from echocardiography is more indicative of the true IVS velocity than either the SCG or ECG.

Both offline and real-time methods for predicting quiescence from SCG perform similarly and both are more accurate than ECG prediction, the current standard gating method. The consistency of the performance between offline and real-time SCG suggests that either can be used depending on the application. Offline SCG-based prediction would not require SCG hardware to be integrated with the CT scanner but would require extra total exam time because of the necessary SCG preliminary exam. Real-time SCG-based prediction, would not require a preliminary exam but would require some interface to communicate the adaptive gating parameters to the CT machine during a CTCA exam.

Quiescence prediction from the ECG performed the worst in terms of both time and deviation error. This suggests that there is room for improvement for gating CTCA acquisition. Although, the effect of lower prediction error on resulting diagnostic quality is a topic for future work, lower deviation error corresponds to less cardiac motion during acquisition and lower time error corresponds to less variance in the position of the heart during the multiple CTCA slice acquisitions taken during an exam. Taken together, lower e_t and e_d will result in improved diagnostic quality of the coronary vessels insofar as IVS motion observed from B-mode echocardiography correspond to coronary vessel motion. From Section 2.2 and [44], IVS motion is a suitable indication for aggregate vessel motion. Thus, prediction methods based on cardiac motion should provide an increase in CTCA diagnostic quality over standard ECG methods for cardiac gating.

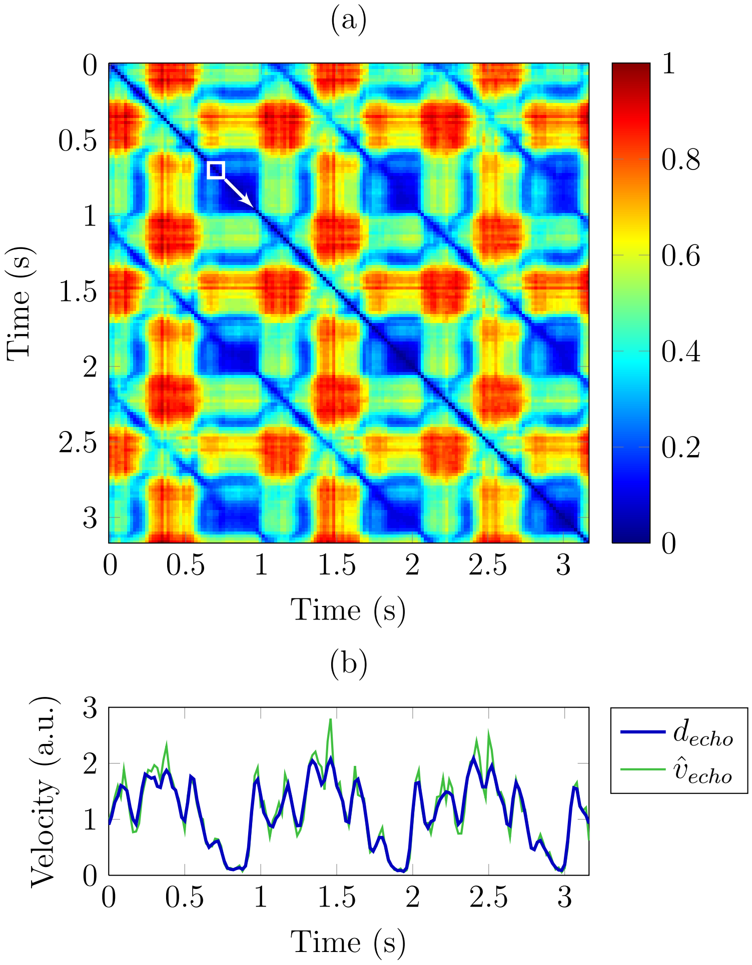

Figure 28: Image demonstrating the calculation of the deviation signal used to assess quiescence predictive performance with the square neighborhood used for averaging shown in white (a). The output of the moving averager, d_{echo}, is shown in (b) along with the approximated velocity, $\hat{v}_{echo}$, calculated as described in Section 2.1.1.1. Both signals in (b) are normalized to have a minimum of zero and a mean of one.

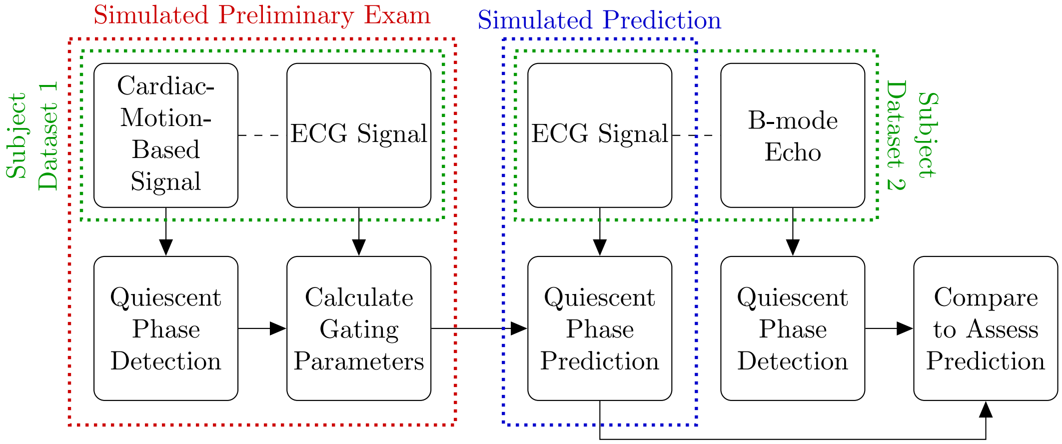

Figure 29: Overview of the analysis flow for offline prediction of cardiac quiescence. Dashed lines connecting data sources indicate synchronously acquired data.

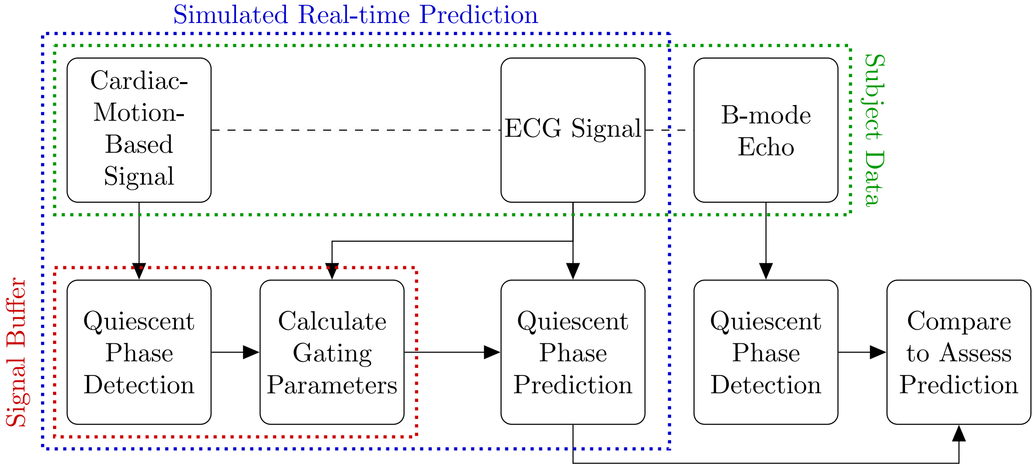

Figure 30: Overview of the analysis flow for real-time prediction of cardiac quiescence. Dashed lines connecting data sources indicate synchronously acquired data.

CHAPTER IV

IMPACT

The intended impact of this work is to demonstrate that ECG alone is a suboptimal predictor and that there is the potential for marked improvement in the gating of CTCA by incorporating signals derived directly from cardiac motion, i.e., echocardiography and SCG. Throughout Chapter 2, significant inter-subject variability was observed suggesting that there is a need for personalized gating for CTCA. The methods used by a clinical CT scanner for predicting cardiac quiescence were demonstrated to be suboptimal in terms of diagnostic image quality of the coronary vessels. Lastly, the simulated gating methods presented in Chapter 3 were shown to achieve superior performance in both the timing and minimization of cardiac motion when compared to ECG gating alone.

In addition, a further preliminary studies was performed. Synchronous ECG, SCG, and echocardiography data were acquired from three subjects receiving cardiac CT exams, allowing for the comparison of cardiac-motion-based signals against the motion observed from CT. This comparison is made to suggest that echocardiography and SCG accurately reflect cardiac motion observed from CT.

4.1 Comparison of Echocardiography and SCG to Cardiac CT

Echocardiography and SCG data were synchronously acquired from three patients receiving cardiac CT exams, allowing for comparisons between echocardiography- and SCG-derived motion information to that obtained from cardiac CT for the same subject.

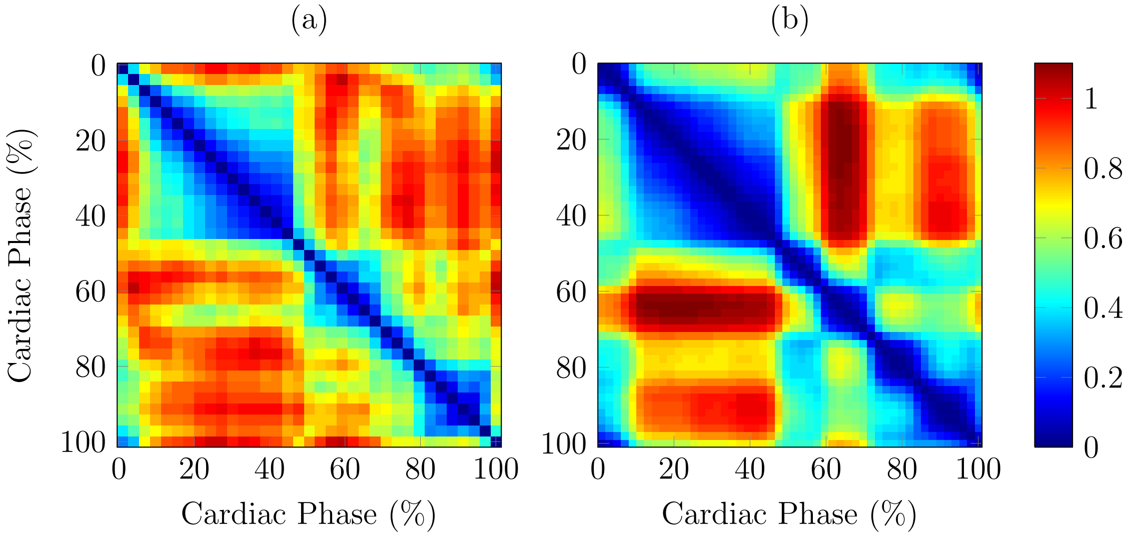

Figure 31: Comparison of deviation matrices from echocardiography (a) and CT (b).

The deviation matrices of both echocardiography and cardiac CT data were calculated as described in Sections 2.1 and 2.2, respectively. An example showing the agreement between the two modalities for the same subject is shown in Figure 31. To compare the cardiac motion based signals used to detect quiescent periods from each modality, the approximated velocity from SCG, echocardiography, and CT are plotted for each of the three subjects in Figure 32. The SCG for Subject 3 was unusable due to low signal amplitude. This was the only instance of the SCG being unusable and the subject had the highest body mass index of all the subjects for this work.

From Figure 32, a general agreement between echocardiography and CT can be seen. This suggests that echocardiography is a suitable tool for analyzing cardiac quiescence. However, it should be stressed that this preliminary study is intended to outline the comparisons and analysis that would be carried out with a larger subject population. With this larger population, the agreement between the quiescent phases detected and predicted from echocardiography and SCG can be compared to the quiescent phases detected from the CT data of the same patient.

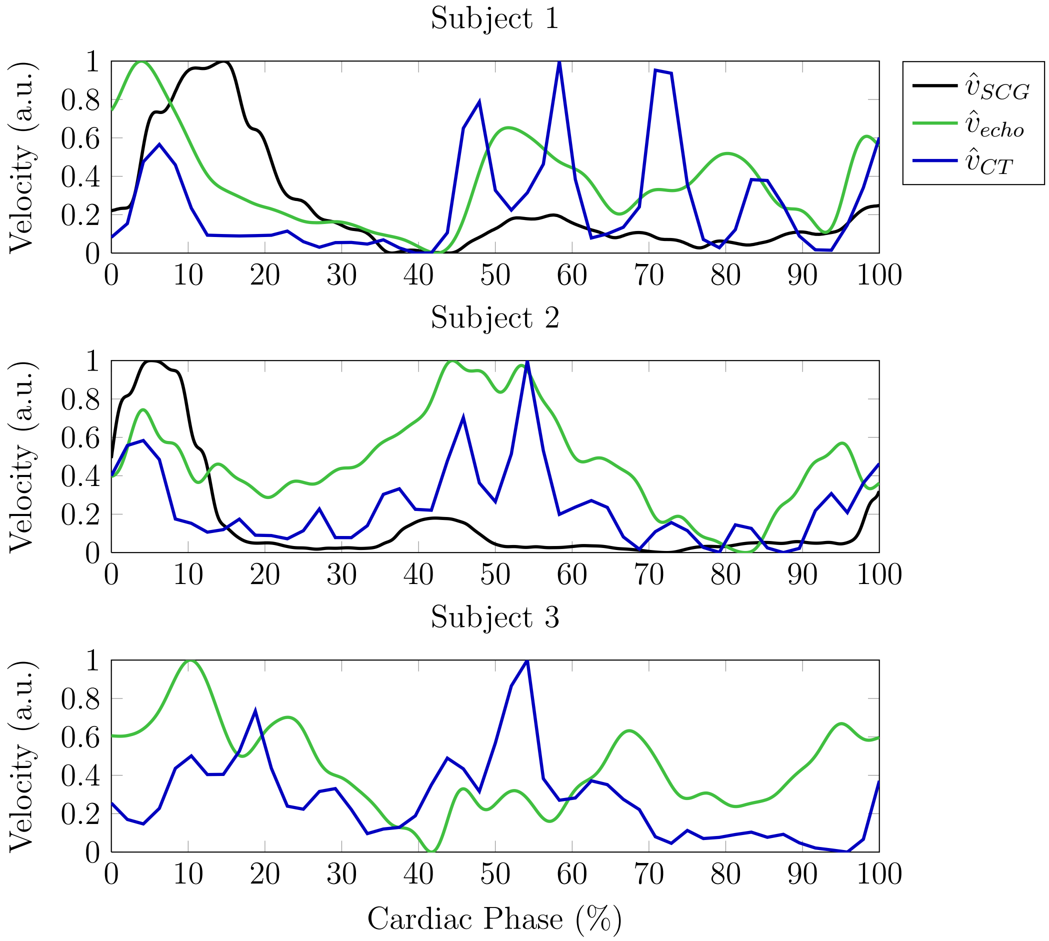

Figure 32: Comparison of the velocity signals from SCG, echocardiography, and CT for Subjects 1, 2, and 3.

CHAPTER V

FUTURE WORK

The material presented in this thesis suggests numerous avenues for future work. These topics fall in a wide range of fields, from digital signal processing to hardware design to clinical implementation. A brief summary of suggested directions for future work follows.

The two most crucial items to be addressed in future work are increasing the number of subjects observed and quantifying the potential improvement in diagnostic quality resulting from any novel quiescence detection and prediction techniques developed. Because CT requires patient radiation, a higher level of confidence in new gating methods is needed prior to implementing cardiac motion based gating on a large scale. That being said, there are numerous ways to bridge this implementation gap. The first step should be to perform preliminary exams similar to those suggested in Section 3.3 to obtain patient-specific gating parameters. Initially, this can be done retrospectively as demonstrated in Section 4.1, where patients already receiving retrospective cardiac CT exams can be examined for SCG and echocardiography. The diagnostic quality of the phases predicted by SCG and echocardiography can then be obtained from the actual CT data allowing for the actual improvement in diagnostic quality to be estimated.

Another possible area for further study is the reliability of the SCG as a tool for observing cardiac motion in the context of cardiac gating for a larger subject population. This reliability is related to the SCG signal power. Thus, a study of the SCG signal strength as a function of various biometrics is suggested. For patients with low SCG signal strength, it will be beneficial to use an accelerometer with less sensor noise than the accelerometer used for this thesis. Lastly, because the SCG is sensitive to subject motion, a method for fusing the quiescent phases predicted in real time from SCG and ECG should be developed. The relative weighting between SCG and ECG parameters would be a function of the confidence in the SCG signal which could be determined from the residual of the Kalman filter as described in Section 2.3.1.1.

APPENDIX A

THEORETICAL EXAMPLE OF FRAME-TO-FRAME DEVIATION FOR B-MODE ECHOCARDIOGRAPHY

To better understand the relationship between the frame-to-frame deviation measure used to detect cardiac quiescence from echocardiography and cardiac feature velocity, it is useful to look at a simple theoretical example. Consider two frames of B-mode echocardiography data, i and j, containing a cardiac feature of interest moving a distance d. Assume the feature is rigid and moves linearly between frames. Lastly, let the image intensities inside the feature, I_{in}, and outside the feature, I_{out}, be constant and let A_{frame} be the area of the frame over which correlation is to be calculated, $A_{feature}$ be the area of the feature of interest, and $A_{overlap}$ be the area of feature overlap between frames. These definitions are shown graphically in Figure 33.

Given the assumptions above, it can be shown that for the B-mode correlation-based deviation measure in (3) that

$$\mathbf{D}(i,j) = 1 - \frac{A_{overlap}A_{frame} - A_{feature}^2}{A_{feature}A_{frame} - A_{feature}^2}, \tag{41}$$

where $\mathbf{D}(i,j)$ is the frame-to-frame deviation measure for a static correlation between frames i and j. Because A_{frame} and $A_{feature}$ are constant, $\mathbf{D}(i,j)$ is only a function of $A_{overlap}$, which depends on the geometry and the displacement of the feature. Also of note, is that this measure is independent of scale.

If the feature is circular, $A_overlap$ will be independent of the direction of the displacement and can be expressed as twice the area of the appropriate circular segment

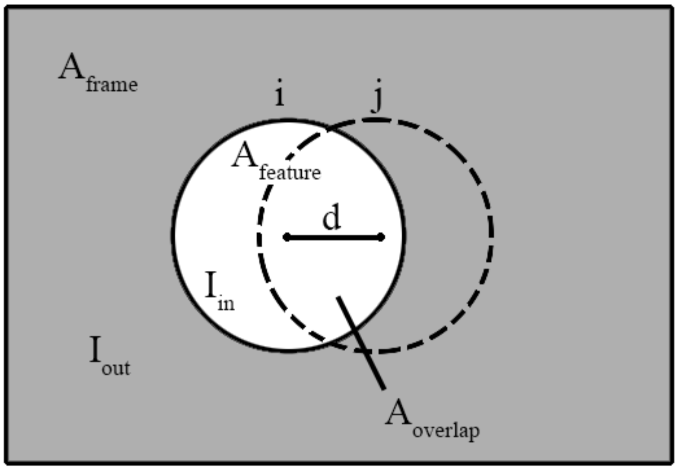

Figure 33: Definition of terms used in the theoretical example relating frame-to-frame B-mode deviation measures to feature velocity. The solid outline indicates the feature in frame i and the dashed outline indicates the feature in frame j, where the feature is displaced a distance of d.

as shown below.

$$A_{segment}(d) = r^2 \cos^{-1}\left(\frac{d/2}{r}\right) - \frac{d}{2}\sqrt{r^2 - \left(\frac{d}{2}\right)^2}, \tag{42}$$

$$\begin{aligned} A_{overlap}(d) &= 2 \cdot A_{segment}(d), \\ &= 2r^2 \cos^{-1}\left(\frac{d}{2r}\right) - \frac{d}{2}\sqrt{4r^2 - d^2}, \end{aligned} \tag{43}$$

where d is the feature displacement between the frames and r is the radius of the circle. Assuming linear motion between two consecutive frames i and j, the displacement d is related to the feature velocity by

$$v(i) = d(i) \cdot f_{FR} \cdot (j - 1), \tag{44}$$

where $v(i)$ is the magnitude of the feature velocity and f_{FR} is the frame rate. $A_{overlap}$ for a circle, Eq 43, is shown in Figure 34 as function of the ration of the displacement to the radius, d/r. Figure 34 shows that for small d relative to r, $A_{overlap}$ is very nearly linear. Because the velocity, $v(i)$, is linearly related to displacement, $d(i)$, this results in a linear relationship between feature velocity and the correlation-based deviation measure, $\mathbf{D}(i, j)$.

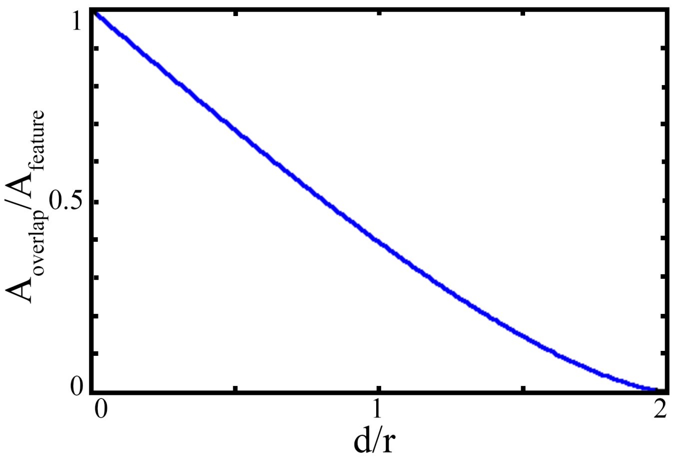

Figure 34: Normalized area of overlap, $A_{overlap}$, for a circle as a function of the ratio of the displacement, d, to the feature radius, r. For small displacement ($d/r < 1$), the function is very nearly linear. When $d \geq 2r$ the overlapping area will be zero.

Given the linearity of displacement, and subsequently velocity, with each deviation matrix, the following relation holds,

$$v(i) \propto \mathbf{D}(i,j) \cdot f_{FR} \cdot (j-i). \tag{45}$$

Assuming the motion is near linear during one sampling period, the velocity can be approximated by

$$v_{\mathbf{D}} = \mathbf{D}(i, i-1). \tag{46}$$

The true velocity can then be expressed as a linear function of $v_{\mathbf{D}}$ as

$$v(i) = \alpha v_{\mathbf{D}}(i) + \beta, \tag{47}$$

where α and β are fitting constants. If provide a reference velocity, $v_{ref}(i)$, the fitting constants α and β can be expressed in a least squares sense as

$$\begin{aligned} \alpha &= \frac{(v_{\mathbf{D}} - \overline{v}_{\mathbf{D}})^T (v_{ref} - \overline{v}_{ref})}{(v_{\mathbf{D}} - \overline{v}_{\mathbf{D}})^T (v_{\mathbf{D}} - \overline{v}_{\mathbf{D}})} \\ &= \frac{\text{covar}(v_{\mathbf{D}}, v_{ref})}{\text{var}(v_{\mathbf{D}})}, \end{aligned} \tag{48}$$

$$\beta = \overline{v}_{ref} - \alpha \overline{v}_{\mathbf{D}}, \tag{49}$$

where $\overline{v}_{\mathbf{D}}$ and $\overline{v}_{ref}$ are the means of $v_{\mathbf{D}}$ and v_{ref}, respectively.

REFERENCES

[1] Roger, V. L., Go, A. S., Lloyd-Jones, D. M., Benjamin, E. J., Berry, J. D., Borden, W. B., Bravata, D. M., Dai, S., Ford, E. S., Fox, C. S., Fullerton, H. J., Gillespie, C., Hailpern, S. M., Heit, J. A., Howard, V. J., Kissela, B. M., Kittner, S. J., Lackland, D. T., Lichtman, J. H., Lisabeth, L. D., Makuc, D. M., Marcus, G. M., Marelli, A., Matchar, D. B., Moy, C. S., Mozaffarian, D., Mussolino, M. E., Nichol, G., Paynter, N. P., Soliman, E. Z., Sorlie, P. D., Sotoodehnia, N., Turan, T. N., Virani, S. S., Wong, N. D., Woo, D., Turner, M. B., and American Heart Association Statistics Committee and Stroke Statistics Subcommittee, "Heart disease and stroke statistics–2012 update: a report from the American Heart Association.," *Circulation*, vol. 125, pp. e2–e220, Jan. 2012.

[2] Bruschke, A. V. G., Sheldon, W. C., Shirey, E. K., and Proudfit, W. L., "A half century of selective coronary arteriography.," *Journal of the American College of Cardiology*, vol. 54, pp. 2139–2144, Dec. 2009.

[3] Kohsaka, S. and Makaryus, A. N., "Coronary angiography using noninvasive imaging techniques of cardiac CT and MRI," *Curr Cardiol Rev*, vol. 4, pp. 323–330, Nov. 2008.

[4] Rivera-Ruiz, M., Cajavilca, C., and Varon, J., "Einthoven's string galvanometer: the first electrocardiograph.," *Tex Heart Inst J*, vol. 35, no. 2, pp. 174–178, 2008.

[5] Wilson, R. A., Bamrah, V. S., Lindsay, J., Schwaiger, M., and Morganroth, J., "Diagnostic accuracy of seismocardiography compared with electrocardiography for the anatomic and physiologic diagnosis of coronary artery disease during exercise testing.," *Am. J. Cardiol.*, vol. 71, pp. 536–545, Mar. 1993.

[6] Starr, I., Rawson, A. J., and Schroeder, H. A., "Studies on the estimation of cardiac output in man, and of abnormalities in cardiac function, from the heart's recoil and the blood's impacts; the ballistocardiogram," *American Journal of Physiology*, vol. 127, pp. 1–28, 1939.

[7] Inan, O. T., "Recent advances in cardiovascular monitoring using ballistocardiography.," *Conf Proc IEEE Eng Med Biol Soc*, vol. 2012, pp. 5038–5041, 2012.

[8] Salerno, D. M., Zanetti, J. M., and Green, L. A., "Qualitative exercise seismocardiography for detection of moderate and severe multivessel coronary

artery disease," *Journal of the American College of Cardiology*, vol. 15, p. 44A, 1990.

[9] Zanetti, J. M. and Salerno, D. M., "Seismocardiography: a technique for recording precordial acceleration," in *Computer-Based Medical Systems, 1991, Proceedings of the Fourth Annual IEEE Symposium*, pp. 4–9, 1991.

[10] Crow, R. S., Hannan, P., Jacobs, D., Hedquist, L., and Salerno, D. M., "Relationship between seismocardiogram and echocardiogram for events in the cardiac cycle," *American Journal of Noninvasive Cardiology*, vol. 8, no. 1, pp. 39–46, 1994.

[11] Akhbardeh, A., tavakolian, K., Viatcheslav, G., Lee, T., New, W., Kaminska, B., and Trayanova, N., "Comparative analysis of three different modalities for characterization of the seismocardiogram," *Engineering in Medicine and Biology Society, EMBC, 2009 Annual International Conference of the IEEE*, pp. 2899–2903, June 2009.

[12] Edler, I. and Lindström, K., "The history of echocardiography," *Ultrasound Med Biol*, vol. 30, pp. 1565–1644, Dec. 2004.

[13] Kalender, W. A., *Computed Tomography.* Wiley-VCH, July 2011.

[14] Kalender, W. A., "X-ray computed tomography," *Phys Med Biol*, 2006.

[15] Herman, G. T., *Fundamentals of Computerized Tomography: Image Reconstruction from Projections.* Springer, Nov. 2009.

[16] Leschka, S., Wildermuth, S., Boehm, T., Desbiolles, L., Husmann, L., Plass, A., Koepfli, P., Schepis, T., Marincek, B., Kaufmann, P. A., and Alkadhi, H., "Noninvasive coronary angiography with 64-section CT: effect of average heart rate and heart rate variability on image quality," *Radiology*, vol. 241, pp. 378–385, Nov. 2006.

[17] Wu, W., Budovec, J., and Foley, W. D., "Prospective and retrospective ECG gating for thoracic CT angiography: A comparative study," *AJR Am J Roentgenol*, vol. 193, pp. 955–963, Oct. 2009.

[18] Sun, Z. and Ng, K.-H., "Prospective versus retrospective ECG-gated multislice CT coronary angiography: a systematic review of radiation dose and diagnostic accuracy," *Eur J Radiol*, vol. 81, pp. e94–100, Feb. 2012.

[19] Moshage, W. E., Achenbach, S., Seese, B., Bachmann, K., and Kirchgeorg, M., "Coronary artery stenoses: three-dimensional imaging with electrocardiographically triggered, contrast agent-enhanced, electron-beam CT.," *Radiology*, vol. 196, pp. 707–714, Sept. 1995.

[20] Desjardins, B. and Kazerooni, E. A., "ECG-gated cardiac CT," *AJR Am J Roentgenol*, vol. 182, pp. 993–1010, Apr. 2004.

[21] Schueler, B. A., "The AAPM/RSNA physics tutorial for residents: general overview of fluoroscopic imaging," *Radiographics*, vol. 20, pp. 1115–1126, July 2000.

[22] Applegate, R. J., Sacrinty, M. T., Kutcher, M. A., Kahl, F. R., Gandhi, S. K., Santos, R. M., and Little, W. C., "Trends in vascular complications after diagnostic cardiac catheterization and percutaneous coronary intervention via the femoral artery, 1998 to 2007," *JACC Cardiovasc Interv*, vol. 1, pp. 317–326, June 2008.

[23] Patel, M. R., Peterson, E. D., Dai, D., Brennan, J. M., Redberg, R. F., Anderson, H. V., Brindis, R. G., and Douglas, P. S., "Low diagnostic yield of elective coronary angiography," *N. Engl. J. Med.*, vol. 362, pp. 886–895, Mar. 2010.

[24] Agostoni, P. and Biondi-Zoccai, G., "Radial versus femoral approach for percutaneous coronary diagnostic and interventional procedures," *Journal of the American College of Cardiology*, vol. 44, pp. 349–356, 2004.

[25] Chen, S. J. and Carroll, J. D., "3-D reconstruction of coronary arterial tree to optimize angiographic visualization," *IEEE Trans Med Imaging*, vol. 19, pp. 318–336, Apr. 2000.

[26] Nieman, K., Oudkerk, M., Rensing, B. J., van Ooijen, P., Munne, A., van Geuns, R. J., and de Feyter, P. J., "Coronary angiography with multi-slice computed tomography," *Lancet*, vol. 357, pp. 599–603, Feb. 2001.

[27] Hurlock, G. S., Higashino, H., and Mochizuki, T., "History of cardiac computed tomography: single to 320-detector row multislice computed tomography," *Int J Cardiovasc Imaging*, vol. 25, pp. 31–42, Apr. 2009.

[28] Schlosser, T., Hunold, P., Schmermund, A., Kühl, H., Waltering, K.-U., Debatin, J. F., and Barkhausen, J., "Coronary artery calcium score: influence of reconstruction interval at 16-detector row CT with retrospective electrocardiographic gating," *Radiology*, vol. 233, pp. 586–589, Nov. 2004.

[29] Tigges, S., Arepalli, C. D., Tridandapani, S., Oshinski, J., Kurz, C. R., Richer, E. J., Chen, Z., Stillman, A. E., and Raggi, P., "A phantom study of the effect of heart rate, coronary artery displacement and vessel trajectory on coronary artery calcium score: potential for risk misclassification," *J Cardiovasc Comput Tomogr*, vol. 6, pp. 260–267, July 2012.

[30] Manzke, R., Köhler, T., Nielsen, T., Hawkes, D., and Grass, M., "Automatic phase determination for retrospectively gated cardiac CT," *Med Phys*, vol. 31, pp. 3345–3362, Dec. 2004.

[31] Srichai, M. B., Hecht, E. M., Kim, D., Babb, J., Bod, J., and Jacobs, J. E., "Dual-source computed tomography angiography image quality in patients

with fast heart rates," *J Cardiovasc Comput Tomogr*, vol. 3, pp. 300–309, Sept. 2009.

[32] Flohr, T. G., McCollough, C. H., Bruder, H., Petersilka, M., Gruber, K., Süss, C., Grasruck, M., Stierstorfer, K., Krauss, B., Raupach, R., Primak, A. N., Küttner, A., Achenbach, S., Becker, C., Kopp, A., and Ohnesorge, B. M., "First performance evaluation of a dual-source CT (DSCT) system," *Eur Radiol*, vol. 16, pp. 256–268, Feb. 2006.

[33] Khan, M., Cummings, K. W., Gutierrez, F. R., Bhalla, S., Woodard, P. K., and Saeed, I. M., "Contraindications and side effects of commonly used medications in coronary CT angiography," *Int J Cardiovasc Imaging*, vol. 27, pp. 441–449, Mar. 2011.

[34] Mahabadi, A. A., Achenbach, S., Burgstahler, C., Dill, T., Fischbach, R., Knez, A., Moshage, W., Richartz, B. M., Ropers, D., Schröder, S., Silber, S., Möhlenkamp, S., and Working group "Cardiac CT" of the German Cardiac Society, "Safety, efficacy, and indications of beta-adrenergic receptor blockade to reduce heart rate prior to coronary CT angiography," *Radiology*, vol. 257, pp. 614–623, Dec. 2010.

[35] Schäfer, D., Borgert, J., Rasche, V., and Grass, M., "Motion-compensated and gated cone beam filtered back-projection for 3-D rotational X-ray angiography," *IEEE Trans Med Imaging*, vol. 25, no. 7, pp. 898–906, 2006.

[36] Isola, A. A., Grass, M., and Niessen, W. J., "Fully automatic nonrigid registration-based local motion estimation for motion-corrected iterative cardiac CT reconstruction," *Med Phys*, vol. 37, pp. 1093–1109, Mar. 2010.

[37] Isola, A. A., Ziegler, A., Schäfer, D., Köhler, T., Niessen, W. J., and Grass, M., "Motion compensated iterative reconstruction of a region of interest in cardiac cone-beam CT," *Comput Med Imaging Graph*, vol. 34, pp. 149–159, Mar. 2010.

[38] Tang, Q., Cammin, J., Srivastava, S., and Taguchi, K., "A fully four-dimensional, iterative motion estimation and compensation method for cardiac CT," *Med Phys*, vol. 39, pp. 4291–4305, July 2012.

[39] Chen, G.-H., Tang, J., and Leng, S., "Prior image constrained compressed sensing (PICCS): a method to accurately reconstruct dynamic CT images from highly undersampled projection data sets," *Med Phys*, vol. 35, pp. 660–663, Feb. 2008.

[40] Tang, J., Hsieh, J., and Chen, G.-H., "Temporal resolution improvement in cardiac CT using PICCS (TRI-PICCS): performance studies," *Med Phys*, vol. 37, pp. 4377–4388, Aug. 2010.

[41] Chen, G.-H., Tang, J., and Hsieh, J., "Temporal resolution improvement using PICCS in MDCT cardiac imaging," *Med Phys*, vol. 36, pp. 2130–2135, June 2009.

[42] Maass, C., Hofmann, C., and Kachelriess, M., "TRI-PICCS in single source and dual source CT," in *Nuclear Science Symposium Conference Record, NSS/MIC, 2010 IEEE*, pp. 2805–2810, 2010.

[43] Wick, C. A., Su, J.-J., Brand, O., McClellan, J. H., Bhatti, P. T., and Tridandapani, S., "A trimodal system for the acquisition of synchronous echocardiography, electrocardiography, and seismocardiography data," in *Engineering in Medicine and Biology Society, EMBC, 2011 Annual International Conference of the IEEE*, pp. 6911–6914, 2011.

[44] Liu, G., Qi, X.-L., Robert, N., Dick, A. J., and Wright, G. A., "Ultrasound-guided identification of cardiac imaging windows," *Med Phys*, vol. 39, no. 6, pp. 3009–3018, 2012.

[45] Svedlow, M., McGillem, C. D., and Anuta, P. E., "Image Registration: Similarity Measure and Preprocessing Method Comparisons," *IEEE Transactions on Aerospace and Electronic Systems*, no. 1, pp. 141–150, 1978.

[46] Noble, J. A. and Boukerroui, D., "Ultrasound image segmentation: a survey," *IEEE Trans Med Imaging*, vol. 25, pp. 987–1010, Aug. 2006.

[47] Tridandapani, S., Fowlkes, J. B., and Rubin, J. M., "Echocardiography-based selection of quiescent heart phases: Implications for Cardiac Imaging," *Journal of Ultrasound in Medicine*, vol. 24, no. 11, pp. 1519–1526, 2005.

[48] Kass, M., Witkin, A., and Terzopoulos, D., "Snakes: Active contour models," *Int J Comput Vision*, vol. 1, pp. 321–331, Jan. 1988.

[49] Mikic, I., Krucinski, S., and Thomas, J. D., "Segmentation and tracking in echocardiographic sequences: active contours guided by optical flow estimates," *IEEE Trans Med Imaging*, vol. 17, no. 2, pp. 274–284, 1998.

[50] Singh, A., "Optic Flow Computation: A Unified Perspective." IEEE Computer Society, Piscataway, NJ, 1991.

[51] Leymarie, F. and Levine, M. D., "Tracking deformable objects in the plane using an active contour model," *IEEE Transactions on Pattern Analysis and Machine Intelligence*, vol. 15, pp. 617–613, June 1993.

[52] Seifarth, H., Wienbeck, S., Püsken, M., Juergens, K.-U., Maintz, D., Vahlhaus, C., Heindel, W., and Fischbach, R., "Optimal systolic and diastolic reconstruction windows for coronary CT angiography using dual-source CT.," *AJR Am J Roentgenol*, vol. 189, pp. 1317–1323, Dec. 2007.

[53] Weustink, A. C., Mollet, N. R., Pugliese, F., Meijboom, W. B., Nieman, K., Heijenbrok-Kal, M. H., Flohr, T. G., Neefjes, L. A. E., Cademartiri, F., de Feyter, P. J., and Krestin, G. P., "Optimal electrocardiographic pulsing windows and heart rate: effect on image quality and radiation exposure at dual-source coronary CT angiography.," *Radiology*, vol. 248, pp. 792–798, Sept. 2008.

[54] Mondillo, S., Galderisi, M., Mele, D., Cameli, M., Lomoriello, V. S., Zacà, V., Ballo, P., D'Andrea, A., Muraru, D., Losi, M., Agricola, E., D'Errico, A., Buralli, S., Sciomer, S., Nistri, S., Badano, L., and Echocardiography Study Group Of The Italian Society Of Cardiology (Rome, Italy), "Speckle-tracking echocardiography: a new technique for assessing myocardial function," *J Ultrasound Med*, vol. 30, pp. 71–83, Jan. 2011.

[55] Sundar, H., Khamene, A., Yatziv, L., and Xu, C., "Automatic Image-Based Cardiac and Respiratory Cycle Synchronization and Gating of Image Sequences," vol. 5762, no. Chapter 47, pp. 381–388, 2009.

[56] Wick, C. A., Su, J. J., McClellan, J. H., Brand, O., Bhatti, P. T., Buice, A. L., Stillman, A. E., Tang, X., and Tridandapani, S., "A system for seismocardiography-based identification of quiescent heart phases: implications for cardiac imaging," *IEEE Transactions on Information Technology in Biomedicine*, vol. 16, no. 5, pp. 869–877, 2012.

[57] Wick, C. A., McClellan, J. H., Ravichandran, L., and Tridandapani, S., "Detection of Cardiac Quiescence From B-Mode Echocardiography Using a Correlation-Based Frame-to-Frame Deviation Measure," *Translational Engineering in Health and Medicine, IEEE Journal of*, vol. 1, 2013.

[58] Schaap, M., Metz, C. T., van Walsum, T., van der Giessen, A. G., Weustink, A. C., Mollet, N. R., Bauer, C., Bogunović, H., Castro, C., and Deng, X., "Standardized evaluation methodology and reference database for evaluating coronary artery centerline extraction algorithms," *Medical Image Analysis*, vol. 13, pp. 701–714, Oct. 2009.

[59] Rohkohl, C., Bruder, H., Stierstorfer, K., and Flohr, T., "Improving best-phase image quality in cardiac CT by motion correction with MAM optimization.," *Med Phys*, vol. 40, p. 031901, Mar. 2013.

[60] Johnson, K. R., Patel, S. J., Whigham, A., Hakim, A., Pettigrew, R. I., and Oshinski, J. N., "Three-dimensional, time-resolved motion of the coronary arteries," *J Cardiovasc Magn Reson*, vol. 6, no. 3, pp. 663–673, 2004.

[61] Brodoefel, H., Burgstahler, C., Tsiflikas, I., Reimann, A., Schroeder, S., Claussen, C. D., Heuschmid, M., and Kopp, A. F., "Dual-source CT: effect of heart rate, heart rate variability, and calcification

on image quality and diagnostic accuracy.," *Radiology*, vol. 247, pp. 346–355, May 2008.

[62] WICK, C. A., MCCLELLAN, J. H., STILLMAN, A. E., and TRIDANDAPANI, S., "A preliminary evaluation of the potential of seismocardiography as a gating tool for cardiac computed tomography," in *NASCI's 2011 Annual Meeting*, 2011.

[63] WICK, C. A., MCCLELLAN, J. H., BRAND, O., BHATTI, P. T., STILLMAN, A. E., and TRIDANDAPANI, S., "Variation between electrocardiographic and seismocardiographic signatures: implications for cardiac computed tomographic gating ," in *AMA-IEEE Medical Technology Conference 2011*, 2011.

[64] KALMAN, R. E., "A new approach to linear filtering and prediction problems," *Journal of basic Engineering*, vol. 82, no. 1, pp. 35–45, 1960.

[65] BISHOP, G. and WELCH, G., "An introduction to the Kalman filter," *Proc of SIGGRAPH, Course*, vol. 8, pp. 27599–23175, 2001.

[66] SEIFARTH, H., PUESKEN, M., WIENBECK, S., MAINTZ, D., FISCHBACH, R., HEINDEL, W., and JUERGENS, K.-U., "Automatic selection of optimal systolic and diastolic reconstruction windows for dual-source CT coronary angiography.," *Eur Radiol*, vol. 19, pp. 1645–1652, July 2009.